



TITLE:

A multistate stem cell dynamics maintains homeostasis in mouse spermatogenesis

AUTHOR(S):

Nakagawa, Toshinori; Jörg, David J.; Watanabe, Hitomi; Mizuno, Seiya; Han, Seungmin; Ikeda, Tatsuro; Omatsu, Yoshiki; ... Simons, Benjamin D.; Yoshida, Shosei; Nagasawa, Takashi

CITATION:

Nakagawa, Toshinori ...[et al]. A multistate stem cell dynamics maintains homeostasis in mouse spermatogenesis. *Cell Reports* 2021, 37(3): 109875.

ISSUE DATE:

2021-10

URL:

<http://hdl.handle.net/2433/274694>

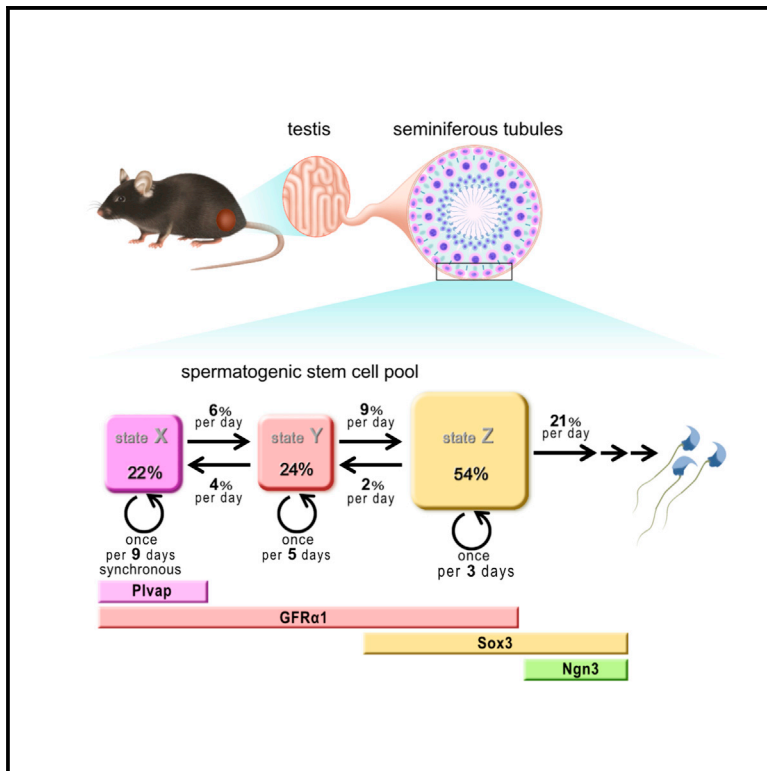
RIGHT:

© 2021 The Author(s); This is an open access article under the Creative Commons Attribution 4.0 International license.

Cell Reports

A multistate stem cell dynamics maintains homeostasis in mouse spermatogenesis

Graphical Abstract



Authors

Toshinori Nakagawa, David J. Jörg, Hitomi Watanabe, ..., Benjamin D. Simons, Shosei Yoshida, Takashi Nagasawa

Correspondence

nakagawa@nibb.ac.jp (T.N.),
shosei@nibb.ac.jp (S.Y.),
tnagasa@fbs.osaka-u.ac.jp (T.N.)

In brief

Nakagawa et al. elucidate the dynamics of mouse spermatogenic stem cells, using a combination of clonal-fate analyses, molecular characterizations, and mathematical modeling. They find that stem cells function as a single heterogeneous pool where commitment for differentiation is not direct but occurs through a reversible transition into differentiation-primed states.

Highlights

- Single pool of heterogeneous stem cells supports homeostasis in mouse spermatogenesis
- Stem cells move reversibly between renewal-biased and differentiation-primed states
- Stem cell dynamics depends on distinct rates of state transition and cell division
- Such multistate dynamics reduces mitotic load, while keeping stem cell density high



Article

A multistate stem cell dynamics maintains homeostasis in mouse spermatogenesis

Toshinori Nakagawa,^{1,2,3,*} David J. Jörg,^{4,5} Hitomi Watanabe,⁶ Seiya Mizuno,⁷ Seungmin Han,^{4,8} Tatsuro Ikeda,¹ Yoshiaki Omatsu,^{3,9} Keiko Nishimura,¹ Miyako Fujita,¹ Satoru Takahashi,^{7,10} Gen Kondoh,⁶ Benjamin D. Simons,^{4,8,11} Shosei Yoshida,^{1,2,12,*} and Takashi Nagasawa^{3,9,*}

¹Division of Germ Cell Biology, National Institute for Basic Biology, National Institutes of Natural Sciences, 5-1 Higashiyama, Myodaiji, Okazaki 444-8787, Japan

²Department of Basic Biology, School of Life Science, Graduate University for Advanced Studies (Sokendai), 5-1 Higashiyama, Myodaiji, Okazaki 444-8787, Japan

³Department of Immunobiology and Hematology, Institute for Frontier Medical Sciences, Kyoto University, 53 Kawahara-cho, Shogoin, Sakyo-ku, Kyoto 606-8507, Japan

⁴The Wellcome Trust/Cancer Research UK Gurdon Institute, University of Cambridge, Tennis Court Road, Cambridge CB2 1QN, UK

⁵Cavendish Laboratory, Department of Physics, J. J. Thomson Avenue, University of Cambridge, Cambridge CB3 0HE, UK

⁶Laboratory of Integrative Biological Science, Institute for Frontier Life and Medical Sciences, Kyoto University, 53 Kawahara-cho, Shogoin, Sakyo-ku, Kyoto 606-8507, Japan

⁷Laboratory Animal Resource Center and Trans-border Medical Research Center, Faculty of Medicine, University of Tsukuba, 1-1-1 Tennodai, Tsukuba, Ibaraki 305-8575, Japan

⁸Wellcome Trust-Medical Research Council Stem Cell Institute, Jeffrey Cheah Biomedical Centre, University of Cambridge, Cambridge CB2 A0W, UK

⁹Laboratory of Stem Cell Biology and Developmental Immunology, Graduate School of Frontier Biosciences and Graduate School of Medicine, World Premier International Immunology Frontier Research Center, Osaka University, 1-3 Yamadaoka, Suita, Osaka 565-0871, Japan

¹⁰Department of Anatomy and Embryology, Faculty of Medicine, University of Tsukuba, 1-1-1 Tennodai, Tsukuba, Ibaraki 305-8575, Japan

¹¹Department of Applied Mathematics and Theoretical Physics, Centre for Mathematical Sciences, Wilberforce Road, Cambridge CB3 0WA, UK

¹²Lead contact

*Correspondence: nakagawa@nibb.ac.jp (T.N.), shosei@nibb.ac.jp (S.Y.), tnagasa@fbs.osaka-u.ac.jp (T.N.)
<https://doi.org/10.1016/j.celrep.2021.109875>

SUMMARY

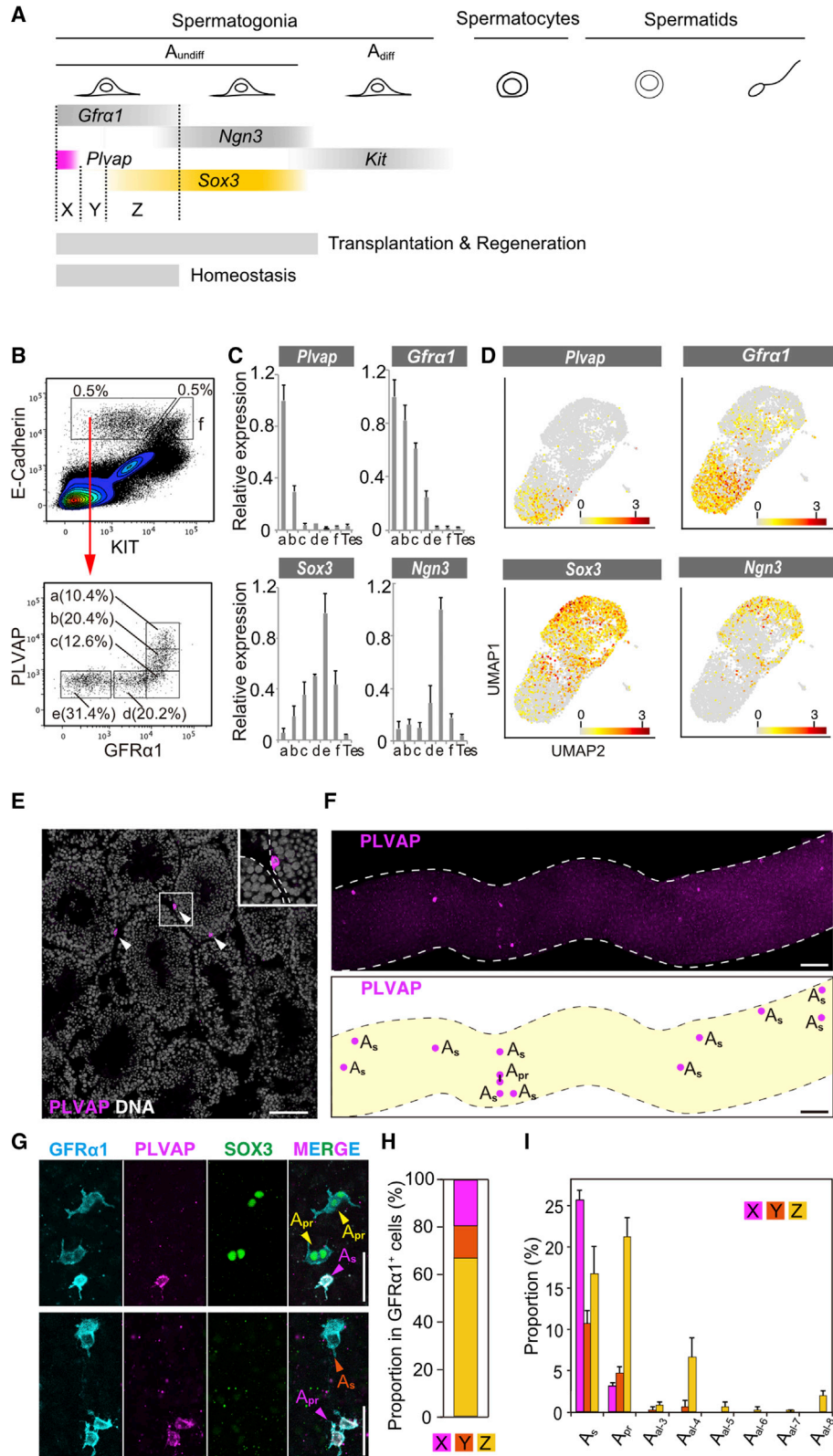
In mouse testis, a heterogeneous population of undifferentiated spermatogonia (A_{undiff}) harbors spermatogenic stem cell (SSC) potential. Although $GFR\alpha1^+ A_{\text{undiff}}$ maintains the self-renewing pool in homeostasis, the functional basis of heterogeneity and the implications for their dynamics remain unresolved. Here, through quantitative lineage tracing of SSC subpopulations, we show that an ensemble of heterogeneous states of SSCs supports homeostatic, persistent spermatogenesis. Such heterogeneity is maintained robustly through stochastic interconversion of SSCs between a renewal-biased $Plvap^+/GFR\alpha1^+$ state and a differentiation-primed $Sox3^+/GFR\alpha1^+$ state. In this framework, stem cell commitment occurs not directly but gradually through entry into licensed but uncommitted states. Further, $Plvap^+/GFR\alpha1^+$ cells divide slowly, in synchrony with the seminiferous epithelial cycle, while $Sox3^+/GFR\alpha1^+$ cells divide much faster. Such differential cell-cycle dynamics reduces mitotic load, and thereby the potential to acquire harmful *de novo* mutations of the self-renewing pool, while keeping the SSC density high over the testicular open niche.

INTRODUCTION

Tissue homeostasis is maintained through the continual replenishment of differentiated cells by residential stem cells. Which cell fraction maintains homeostasis and how are long-standing questions to which multiple hypotheses have been raised. Traditionally, tissue stem cells are thought to comprise a restricted compartment of undifferentiated cells that perfectly self-renew while giving rise to committed cells, which terminally differentiate

either directly or through a limited series of divisions (Watt and Hogan, 2000). In addition, tissue stem cells are often assumed to be slow-cycling, minimizing risks associated with the accumulation of harmful *de novo* mutations arising through DNA replication, and justifying their identification based on label-retaining assays (Cotsarelis et al., 1990; Potten et al., 1974). However, recent studies have challenged these prevailing views: in many tissues, it has been shown that cells normally committed to differentiation can reacquire self-renewal potential in response to





(legend on next page)

Cell Reports

Article



injury or transplantation (de Sousa E Melo and de Sauvage, 2019; Fuller and Spradling, 2007; Hogan et al., 2014; Merrell and Stanger, 2016; Yoshida, 2019). Thus, self-renewal *potential* extends over multiple cell states, questioning whether such cell-state interchange may also contribute during long-term tissue homeostasis. Moreover, the slow-cycling property of tissue stem cell function has also been called into question: for example, while hematopoietic stem cells are shown to be slow cycling (Busch et al., 2015; Cheshier et al., 1999), in the small intestinal epithelium, evidence suggests that label-retaining cells positioned in the vicinity of row +4 in the crypt are destined for differentiation (Buczacki et al., 2013), while the major Lgr5⁺ stem cell compartment divides rapidly (Barker et al., 2007; Buczacki et al., 2013; Snippert et al., 2010).

Mouse spermatogenesis constitutes a typical tissue stem cell-supported process that takes place in testicular seminiferous tubules (Russell et al., 1990; Yoshida, 2019). Spermatogenic stem cell (SSC) function resides within *undifferentiated* spermatogonia (A_{undiff}) that localize on the basement membrane of the tubules, comprising <1% of testicular germ cells. A_{undiff} produces *differentiating* spermatogonia, which further mature into meiotic spermatocytes and haploid spermatids (Figure 1A). The A_{undiff} population is heterogeneous in gene expression, including multiple transcriptional states (La et al., 2018; Yoshida, 2019). Morphologically, germ cells show a second axis of heterogeneity with A_{undiff} comprising singly isolated cells (A_{single} or A_{s}) and syncytia of two (A_{paired} or A_{pr}) or more (A_{aligned} or A_{al}) cells, which result from incomplete cell division maintaining a connection between daughter cells via intercellular bridges (ICB), as well as fragmentation of syncytia via ICB breakdown (Hara et al., 2014; Russell, 1990; Yoshida et al., 2007b). Regarding cell-cycle heterogeneity, a small fraction of label-retaining A_{s} spermatogonia have been observed in rat testis, detectable for 13–19 days after S phase labeling, while in most spermatogonia the label dilutes out much faster (Huckins, 1971a).

The ability of multiple subfractions of A_{undiff} to reconstitute spermatogenesis when transplanted into host seminiferous tubules suggests that SSC *potential* is shared broadly over the A_{undiff} population (Garbuzov et al., 2018; Nakagawa et al., 2007; Nakamura et al., 2021) (Figure 1A). However, these subfractions do not contribute equally to the maintenance of homeostasis. Crucially, lineage-tracing studies using indelible genetic labeling by tamoxifen-inducible Cre indicate that stem cell function is largely restricted to the $\text{GFR}\alpha 1^+$ fraction of A_{undiff} , many of which

are A_{s} or A_{pr} , with negligible, if any, contribution from the $\text{GFR}1^-$ population (Hara et al., 2014). The $\text{GFR}\alpha 1^-$ fraction of A_{undiff} is largely $\text{Ngn}3^+$, which includes many A_{al} and fewer $A_{\text{s}}/A_{\text{pr}}$ and shows consistent expression of *Piwil4* (*Miwil2*) and *RAR* γ . Although contributing significantly to regeneration after insult or transplantation, $\text{Ngn}3^+ A_{\text{undiff}}$ largely differentiates with very small contributions to the self-renewing pool during homeostasis (Carrieri et al., 2017; Ikami et al., 2015; Nakagawa et al., 2007, 2010; Nakamura et al., 2021; Yoshida et al., 2004). While a significant portion of A_{undiff} (quantified at 10% by whole-mount immunofluorescence) is found to be $\text{GFR}\alpha 1^+/\text{Ngn}3^+$ double positive, only a negligible fraction of A_{undiff} (0.1%) is $\text{GFR}\alpha 1^-/\text{Ngn}3^-$ double negative (Nakagawa et al., 2010). Thus, dissecting the behavior of the $\text{GFR}\alpha 1^+ A_{\text{undiff}}$ compartment is key to understanding the mechanisms underpinning tissue homeostasis (Figure 1A).

Alongside their morphological heterogeneity, $\text{GFR}\alpha 1^+ A_{\text{undiff}}$ is also heterogeneous in gene expression (Chan et al., 2014; La et al., 2018; Sharma et al., 2019; Tokue et al., 2017). However, the link between transcriptional heterogeneity and their population dynamics remains in debate (de Rooij, 2017; Lord and Oatley, 2017; Mäkelä and Hobbs, 2019; Yoshida, 2019). Some propose that a distinct subset of A_{undiff} (e.g., $\text{Id}4^{\text{high}} A_{\text{s}}$ cells) comprises a definitive self-renewing compartment (Aloisio et al., 2014; Chan et al., 2014), extending the prevailing “ A_{s} model” that A_{s} cells constitute the SSCs with A_{pr} and A_{al} committed irreversibly to differentiate (Huckins, 1971b, 1971c). On the other hand, through intravital live-imaging and quantitative clonal-fate analyses of $\text{GFR}\alpha 1^+$ cells performed in homeostasis combined with mathematical modeling, our group has proposed that $\text{GFR}\alpha 1^+$ cells comprise a single heterogeneous SSC pool (Hara et al., 2014). Recent advances in single-cell gene-expression profiling have provided rich, albeit static, information about the heterogeneity of A_{undiff} and its short-term dynamics, further questioning the nature of SSC states (La et al., 2018; Suzuki et al., 2021). However, insights into the functional identity of SSCs underpinning long-term homeostasis can only be drawn by integrating such molecular characterizations of cell heterogeneity with experiments that can trace the fate behavior of subfractions of A_{undiff} over time.

Here, by identifying and mapping quantitatively the kinetics of key substates of A_{undiff} using pulse-labeling studies over a range of timescales, we resolve the functional, molecular, and morphological heterogeneity of the SSC compartment during homeostasis.

Figure 1. Heterogeneity of $\text{GFR}\alpha 1^+ A_{\text{undiff}}$ represented by *Plvap* and *Sox3* expression

- (A) Scheme for the process of spermatogenesis with the expression of key genes. X, Y, and Z indicate the fractions of $\text{GFR}\alpha 1^+ A_{\text{undiff}}$ that are the focus of this study (see text for details). The ranges of cells showing the vast majority of SSC function during homeostasis and following transplantation are also indicated.
- (B) FACS plot of cells from adult mouse testes, showing PLVAP and $\text{GFR}\alpha 1$ expression in the A_{undiff} ($\text{E-Cadherin}^+ \text{KIT}^{-/\text{low}}$) gate, with the percentages of each fraction (a–e) out of the total A_{undiff} indicated.
- (C) qRT-PCR analysis of sorted cells in fractions a–f in (B), and whole adult testes (Tes), for indicated.
- (D) UMAPs representing expression of key genes of A_{undiff} (*Plzf-mCherry*⁺*CD9*⁺*KIT*⁻) population from scRNA-seq data of a published study (La et al., 2018); see also Figure S1H. Color bars: \log_2 -transformed normalized UMIs.
- (E) PLVAP⁺ cells (arrows) immunostained on an adult mouse testis section. Inset, a magnified view of the box; dashed lines, basement membrane.
- (F) Whole-mount IF of a seminiferous tubule, with the PLVAP⁺ cell distribution illustrated below.
- (G) Magnified images of whole-mount seminiferous tubules stained for $\text{GFR}\alpha 1$ (cyan), PLVAP (magenta), and SOX3 (green).
- (H and I) Proportions of X, Y, and Z fractions based on whole-mount IF, shown in relation to total cell number (H) and composition, viz. A_{s} , A_{pr} , and A_{al} of different lengths (I).
- Graphs in (C) and (I) indicate mean \pm SD (n = 3). Scale bars, 50 μm in (G) and 100 μm in (E) and (F).

RESULTS

Plvap and Sox3 expression represents subfractions of $GFR\alpha1^+ A_{undiff}$

By comparing gene expression between fractions of A_{undiff} showing different levels of $GFR\alpha1$ expression including $GFR\alpha1^{high}$, $GFR\alpha1^{low}$, and $GFR\alpha1^-$ fractions, we found that cells showing the highest levels of $GFR\alpha1$ were highly enriched in the expression of *Plvap* (encoding a cell-surface protein, Plasma-lemma vesicle-associated protein) (Figures 1B, S1A, and S1B). Developing a fluorescence-activated cell-sorting (FACS) strategy that expands the A_{undiff} (E-Cad⁺/KIT⁻) population based on the levels of surface $GFR\alpha1$ and PLVAP, we found that $GFR\alpha1^+ A_{undiff}$ comprises a continuum in which PLVAP expression is restricted to $GFR\alpha1^{high}$ cells (Figures 1B, S1C, and S1D). Further, qRT-PCR analysis of the sorted subfractions showed that some renewal-related genes (e.g., *Eomes*, *Shisa6*, *Pdx1*, *T*) showed similarly enriched expression patterns, while others (e.g., *Id4*, *Nanos2*) showed broader expression across the $GFR\alpha1^+$ compartment (Figures 1B, 1C, S1E, and S1F) (Chan et al., 2014; La and Hobbs, 2019; Sada et al., 2009; Sharma et al., 2019; Tokue et al., 2017; Yoshida, 2019). By contrast, differentiation-associated genes exhibited opposite gradients within A_{undiff} : *Ngn3* and *Rar γ* showed higher specificity to $GFR\alpha1^- A_{undiff}$ (fraction “e”) compared to *Sox3*, which extended into $GFR\alpha1^+$ compartment (fractions “d,” “c” and, to a lesser extent, “b”) (Figures 1C and S1G) (Gely-Pernot et al., 2012; Ikami et al., 2015; Raverot et al., 2005; Yoshida et al., 2004). Differentiating spermatogonia (fraction “f”) was characterized by *Stra8* and *Kit* expression (Figure S1G) (Yoshinaga et al., 1991; Zhou et al., 2008). These gradients of self-renewal and differentiation-related gene expression were consistent with the results of a recent single-cell RNA sequencing (scRNA-seq) study of A_{undiff} purified based on *Plzf*-mCherry expression (La et al., 2018); the data were also reanalyzed in this study verifying such linear gradients (Figures 1D and S1H).

In testis tissue, immuno-detected PLVAP⁺ spermatogonia were scattered sparsely on the basement membrane of seminiferous tubules (Figures 1E and 1F), with biased localization to the interstitium, in common with reported A_{undiff} fractions (Figures S2A–S2C) (Chiarini-Garcia et al., 2001; Hara et al., 2014; La et al., 2018; Yoshida et al., 2007b). Consistent with the RNA analyses described above, multi-staining of whole-mount seminiferous tubules revealed that overlapping, albeit not identical, expression of signature proteins (e.g., PLVAP, PDX1, and T) characterized a “most undifferentiated” fraction of $GFR\alpha1^+$ cells, in which PLVAP showed the most restricted expression (Figures S2D and S2E). Similarly, in parallel with RNA, high levels of SOX3 protein were also observed in $GFR\alpha1^+/NGN3^+ A_{undiff}$; lower but significant expression was also detected in a fraction of $GFR\alpha1^+ A_{undiff}$ in which $GFR\alpha1$ was expressed at lower levels compared with $GFR\alpha1^+/SOX3^-$ cells (Figures S2F and S2G). With the detection thresholds of our whole-mount IF, we found a significant number of $GFR\alpha1^+/PLVAP^+/SOX3^-$ cells, while $GFR\alpha1^+/PLVAP^+/SOX3^+$ cells were barely observed.

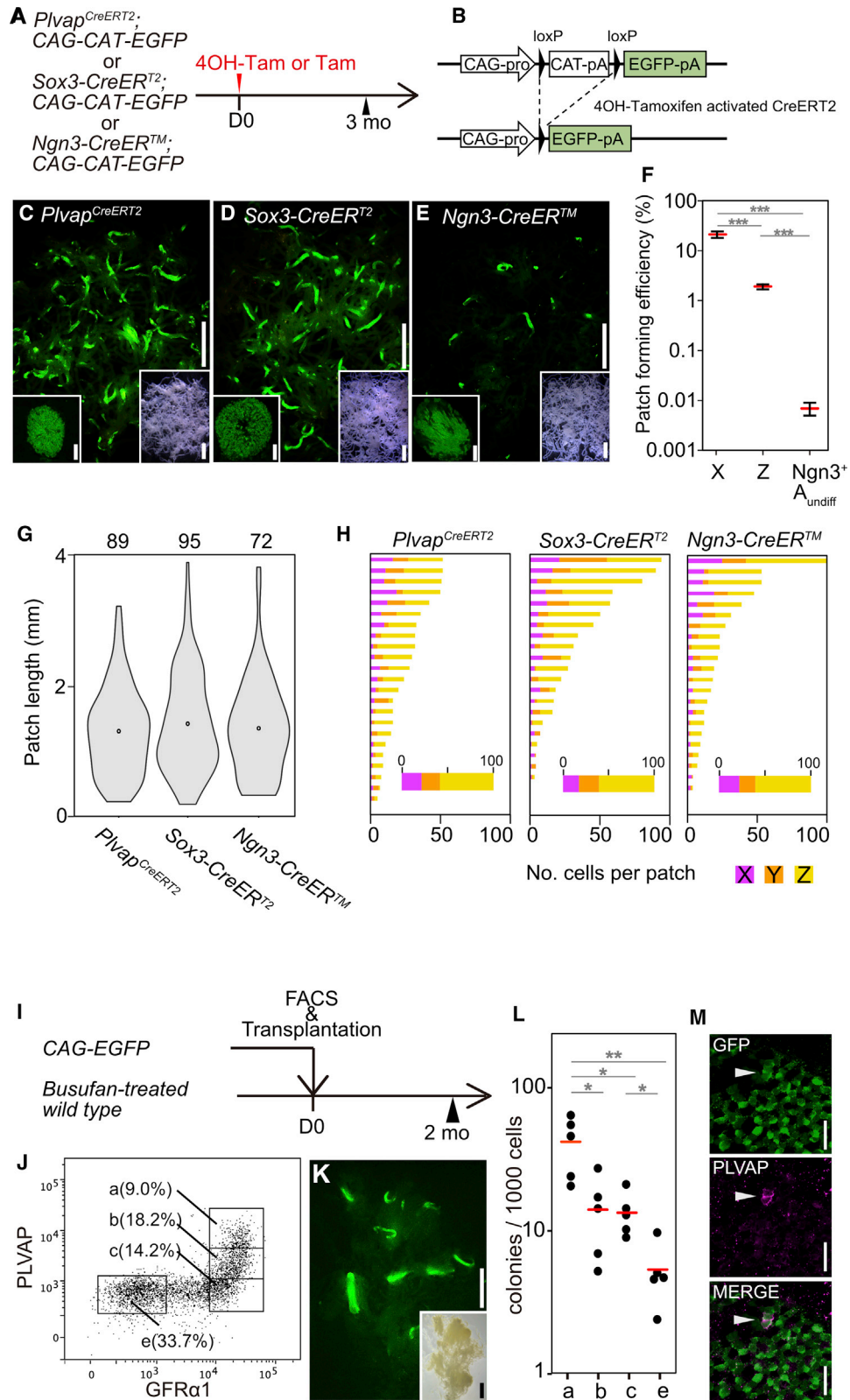
Based on these observations, we divided the $GFR\alpha1^+$ compartment into PLVAP⁺ (designated for brevity as “X”), PLVAP⁻/SOX3⁻ (“Y”), and SOX3⁺ (“Z”) fractions (Figures 1A,

1G, and 1H). Morphologically, the vast majority of X cells were A_S , with a few A_{pr} . Y included less A_S and more A_{pr} , as well as some A_{al-4} ; Z was further tilted toward longer syncytia including some A_{al-4} and A_{al-8} (Figure 1I). In Y and Z fractions, A_{al} with cell numbers other than the canonical 2^n were also observed (e.g., A_{al-3} in Y; $A_{al-3, 5, 6, 7}$ in Z). Clustering analysis of the published scRNA-seq data (La and Hobbs, 2019) showed that states X and Z were characterized by the expression of signature genes including *Plvap* and *Sox3*, respectively (Figures S1I–S1L). Yet, Y cells appeared not to show a unique gene-expression signature but were characterized by low levels of X- and Z-related genes (Figures S1J, S1M, and S1N). Together, within the $GFR\alpha1^+$ compartment, X cells showed “the most undifferentiated” gene-expression profile and “primitive” morphology, while the Z cells were inclined for differentiation, with the Y population laying in between (Figure 1A).

An ensemble of multiple fractions of $GFR\alpha1^+ A_{undiff}$ supports homeostasis

To follow the fate behavior of $Plvap^+$ and $Sox3^+$ cells in homeostasis, we then generated *Plvap^{CreERT2}* and *Sox3-CreERT2* alleles, which mediate faithful cell-specific recombination (Figures S3A–S3R). Using these alleles, we pulse-labeled $Plvap^+$ and $Sox3^+$ cells irreversibly with GFP expression by 4OH-tamoxifen administration in adult mice (Figures 2A and 2B). For comparison, the fate of $Ngn3^+$ cells was also analyzed using a previously developed *Ngn3-CreERTTM* allele (Yoshida et al., 2006) (Figure 2A). Three months after the pulse, patches of GFP⁺ cells comprising all stages of spermatogenesis were formed, indicating their contribution to long-term spermatogenesis in homeostasis (Figures 2C–2E). However, the frequency of long-term patch formation varied greatly between fractions: compared to X cells, Z and $GFR\alpha1^-$ cells showed a survival potential that was around 1 and 3 orders of magnitude lower, respectively (Figure 2F; Data S1). Notably, despite such divergent potential, the resultant patches showed a statistical size distribution (i.e., the spatial extent of their progenies) indistinguishable irrespective of the original cell state (Figure 2G). Further, virtually all the patches harbored X, Y, and Z cells at proportions consistent with the tissue average, once again irrespective of the original state. Differences were only seen in very small clonal patches that may be in the process of becoming “extinct” through differentiation (Figure 2H). These findings suggest that, during homeostasis, X, Y, and Z fractions of $GFR\alpha1^+ A_{undiff}$ undergo mutual state transitions, maintaining robustly the heterogeneous cell composition. By contrast, $Ngn3^+$ cells make only a very small, albeit non-zero, contribution to homeostasis, as reported previously (Nakagawa et al., 2007).

Next, to examine the SSC potential of cells in different states of A_{undiff} , we transplanted cell fractions sorted based on surface $GFR\alpha1$ and PLVAP levels (Figures 2I and 2J) into the host seminiferous tubules whose germ cells had been depleted, and the resultant repopulating colonies were counted 2 months later (Figures 2K, 2L, and S3S) (Brinster and Zimmermann, 1994). The results revealed that the transplantable SSC potential is shared broadly over A_{undiff} , with a gradient in which a fraction of cells that roughly corresponds to the X compartment (fraction “a”; Figure S3T) and the fraction of $GFR\alpha1^- A_{undiff}$ (“e”) show the



(legend on next page)

highest and lowest efficiencies, respectively (Figure 2L). Although this trend parallels with their long-term patch-forming efficiencies during homeostasis, the difference between fractions were much smaller in the case of transplantation. In particular, fraction “e” showed only a 1 order of magnitude lower transplantation efficiency compared with fraction “a.” However, in homeostasis, Ngn3⁺ cells (mostly GFR α 1⁻ A_{undiff}) showed about 3 orders of magnitude lower patch-forming frequency relative to Plvap⁺ (X) cells (Figure 2F). Regardless of the original state, all resultant colonies included PLVAP⁺ cells, evidencing the reverse transition into a Plvap⁺ state when transplanted Plvap⁻ cells form colonies (Figures 2M and S3S), again reminiscent of the observation in long-term patches (Figure 2H).

To summarize, the rate of long-term self-renewal varies between fractions of A_{undiff}, with Plvap⁺ (X) cells (and fraction “a”) showing the highest efficiency. However, the relative efficiencies depend greatly on the tissue context; much broader fractions contribute efficiently to self-renewal in regeneration than in homeostasis. This agrees with, and extends, previous observations where the heterogeneity of the GFR α 1⁺ population was not considered (Nakagawa et al., 2007; Nakamura et al., 2021; Yoshida et al., 2007a).

Plvap⁺ cells reside at the top of a differentiation hierarchy and follow divergent fate behavior

We then investigated the fate behavior of individual Plvap⁺ (X) cells during homeostasis, following pulse-labeling at clonal density using a low dose of 4OH-tamoxifen (Figures 3A–3G). Over the course of 20 days post-labeling, whole-mount tubule specimens were quadruple stained for PLVAP, GFR α 1, SOX3, and GFP (the lineage marker). Then, GFP-labeled clones were scored by the number and syncytial lengths of constituent GFP⁺ cells and classified into X, Y, Z, and more advanced (GFR α 1⁻) cells (Figures 3B and 3C; Table S1 for complete dataset). Immediately following the pulse, induced cells (GFP⁺) were observed predominantly in state X, as expected, but subsequently spread to Y, Z, and GFR α 1⁻ fractions with their first appearance in chronological order, i.e., on days 1, 2, and 4, respectively (Figures 3D and 3E). Therefore, in homeostasis, the X, Y, Z, and GFR α 1⁻ states comprise a functional hierarchy

arranged in this order. Although other lineage trajectories (e.g., X-to-Z or Y-GFR α 1⁻) cannot be ruled out, these were not evidenced by experiment.

At the clonal level, pulse-labeled Plvap⁺ cells followed highly variable fates. The portion of clones that lost all X cells progressively increased, while others gained an increasing number of X cells. Further, labeled clones comprised cells with variable gene expression (X, Y, Z, and/or GFR α 1⁻) and morphologies, greatly increasing the complexity of their clonal composition over time (Figure 3F; Table S1). Of particular note, however, the overall ratio of X, Y, and Z cells and their morphological compositions, when averaged over the labeled (GFP⁺) cells, converged to homeostatic values within 14–20 days (Figure 3G). This indicates that the labeled cells rapidly spread over the GFR α 1⁺ compartment in a representative manner.

Sox3⁺ cells revert to Plvap⁺ state and contribute to long-term self-renewal in homeostasis

We then analyzed the fate of pulse-labeled Sox3⁺ cells in homeostasis. Since the abundance of Sox3⁺/GFR α 1⁻ cells prevented their clonal-fate analysis, we examined their fate behavior at the population level (Figures 3H–3K). As an innate limitation of the pulse-labeling assay, there is a delay (of around 2 days) before labeled cells can be identified by detecting the accumulated GFP protein. To overcome this constraint, we detected RNA transcribed from the recombined allele by RT-qPCR using cell fractions sorted 12 h after 4OH-tamoxifen injection. The results verified a high recombination specificity of the Sox3-CreER allele, with no evidence of recombination in X cells (Figures S4A–S4D). Two days after pulse, when labeled cells were detectable using whole-mount IF for GFP protein, a large fraction (~33%) of Z cells were found to be GFP⁺, while labeled cells were also observed in Y and X fractions at lower frequencies (Figures 3I and 3K). By day 10, the labeled fraction of Z cells had greatly decreased as they differentiated and were replenished by unlabeled cells from the X and Y compartments (Figures 3J and 3K). During this period, the labeled fractions of X and Y cells were increased; 3 months after induction, X, Y, and Z fractions were labeled equally (Figure 3K). These findings indicate that, following pulse-labeling, some Sox3⁺ cells revert to Y and X

Figure 2. Contribution of Plvap⁺ and Sox3⁺ cells to long-term spermatogenesis during homeostasis

(A) Experimental scheme for (C)–(H), analyzing repopulating patch formation over the long term, using Plvap^{CreERT2}, Sox3-CreERT², and Ngn3-CreERTTM mice (see Data S1 for details).

(B) Structure of CAG-CAT-EGFP transgene (Kawamoto et al., 2000). Tamoxifen injection to mice carrying CreER and CAG-CAT-EGFP genes induces temporary Cre activity, leading to indelible EGFP expression under a ubiquitous CAG promoter by deleting intervening CAT-poly(A) sequence.

(C–E) Fluorescence microscopy of untangled seminiferous tubules from Plvap^{CreERT2} (C), Sox3-CreERT² (D), and Ngn3-CreERTTM (E) mouse testes 3 months after pulse, showing patches of GFP⁺ cells. Insets, bright-field images of untangled tubules and cross-sections of GFP⁺ patches.

(F) Long-term patch-forming efficiency of X, Z, and Ngn3⁺ A_{undiff}, based on the numbers of initially labeled cells 2 days after pulse and patches 3 months after pulse, with red lines indicating mean derived from 5, 3, and 6 mice, respectively (see Data S1 for detailed calculation).

(G) Violin plots showing length distributions of patches observed in indicated mice, 3 months after the pulse, with dots indicating mean from patches of indicated numbers analyzed.

(H) Numbers of X, Y, and Z cells in each of 24 randomly selected patches observed in each mice 3 months after pulse. Proportions summed over all 24 patches are shown as thick bars.

(I) Experimental scheme for (J)–(M), assessing the colony formation of sorted A_{undiff} fractions following transplantation.

(J) FACS plot of E-Cadherin⁺KIT^{-low} A_{undiff} from CAG-EGFP mouse testes for transplantation into germ-cell depleted testes of wild-type mice.

(K) Representative image of fluorescence intensity of recipient testis 2 month after transplanting fraction “a.” Inset, bright-field image.

(L) Colony-forming efficiency of sorted fractions (per 1,000 donor cells), with red lines representing means.

(M) Emergence of PLVAP⁺ cells 2 months after transplanting GFP⁺ cells of fraction “c” (arrowhead).

Scale bars, 2mm in (C–E) and (K), 50 μ m in left insets of (C)–(E) and (M); *p < 0.05, **p < 0.01, ***p < 0.001, respectively (t test).

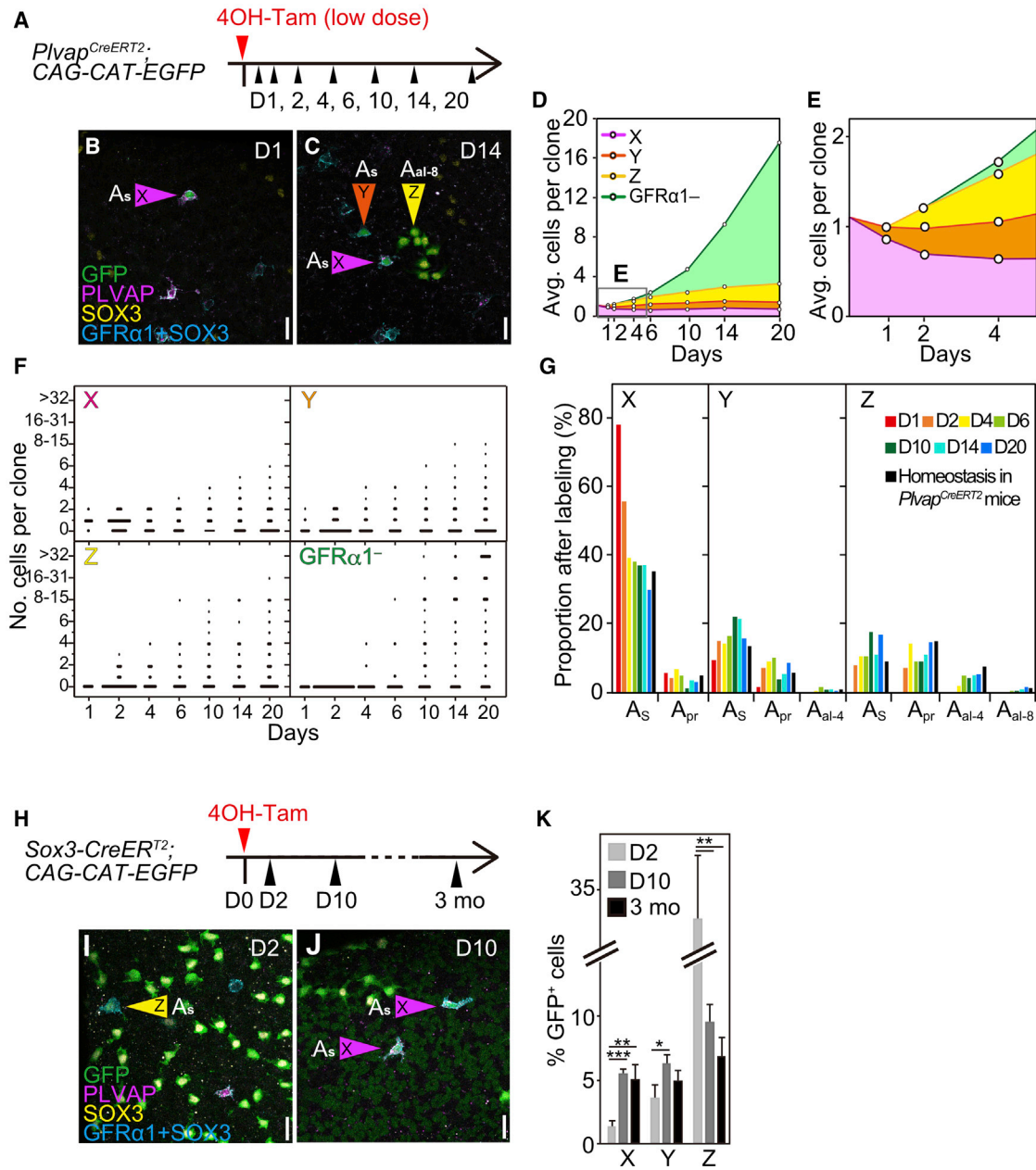


Figure 3. Fate analyses of *Plvap*⁺ and *Sox3*⁺ cells during homeostasis

(A) Scheme for clonal-fate analysis of pulse-labeled *Plvap*⁺ cells in (B)–(G). *Plvap*⁺ cells were pulse-labeled at clonal density with low dose of 4OH-Tamxifen, and their progenies were analyzed at indicated time points.

(B and C) Whole-mount IF of the seminiferous tubules 1 and 14 days after induction.

(D and E) Kinetics of average clone composition following induction (D), with the region at early time points indicated by gray box shown expanded in (E).

(F) Distribution of clone size, indicated by the number of X, Y, Z, and *GFRα1*[−] cells contained in each clone (dot) over time.

(G) Kinetics of the overall composition of the pulse-labeled *Plvap*⁺ cells, compared with those based on the homeostatic tissue average. *A_{al}* composed of other than 2ⁿ cells are omitted given their low abundance (see Figure S5D).

(H) Scheme for fate analysis of pulse-labeled *Sox3*⁺ population in (I)–(K).

(I–J) Whole-mount IF images of the seminiferous tubules 2 and 10 days after induction.

(K) Portion of GFP⁺ cells in the X, Y, and Z fractions at indicated time points, shown as mean ± SEM (n = 3).

Scale bars, 30 μm; *p < 0.05, **p < 0.01, ***p < 0.001, respectively (t test).

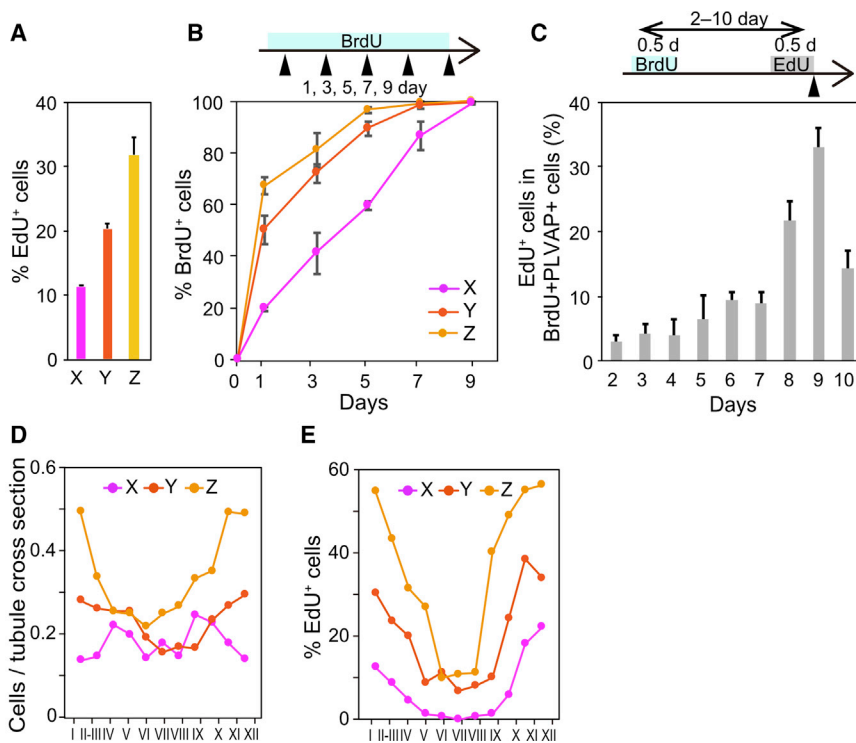


Figure 4. Cell-cycle properties of X, Y, and Z cells in relationship to the seminiferous epithelial cycle

(A) Percentages of EdU⁺ cells in X, Y, and Z fractions 1 h after a single pulse of EdU, shown as mean \pm SD (n = 4 testes).

(B) Continuous BrdU labeling, with schedule as depicted. The kinetics of BrdU incorporation in the cells of the X, Y, and Z fractions are shown as mean \pm SD (n = 3).

(C) Sequential pulse labeling with BrdU and EdU with variable lengths of intervals, following the schedule shown, followed by whole-mount IF analyses for PLVAP, BrdU, and EdU. Percentages of EdU⁺ cells in BrdU⁺ PLVAP⁺ cells at indicated time points are shown as mean \pm SD (n = 3).

(D and E) Frequency of X, Y, and Z cells along the seminiferous epithelial cycle (D) and percentage of EdU⁺ cells in these fractions shortly (15 h) after EdU pulse (E). A total of 9,468 tubular sections from three testes were analyzed.

states, consistent with the contribution of Sox3⁺ cells to long-term homeostasis (Figure 2D).

On the other hand, pulse-labeled Ngn3⁺ cells, some of which were initially GFR α 1⁺ reflecting the small number of GFR α 1⁺/Ngn3⁺ cells, lost GFR α 1 expression quickly in virtually all descendant cells (Figure S4E), compatible with their very low patch-forming efficiency (Figure 2F). Therefore, within the Sox3⁺ cell population, Z cells make the largest contribution to the GFR α 1⁺ compartment and long-term self-renewal.

The ability of Plvap⁻ cells to contribute to the Plvap⁺ (X) cell compartment in homeostasis is further supported by an independent and deeper analysis of the fate of X cells. First, we found that labeled X cells did not perfectly self-renew; instead, descendants of induced X cells maintained only about 70% of the X cell population over the long term, while the remainder (~30%) were “recovered” from outside the X compartment (Figures S4F and S4G). Further, given the results of a previous intravital live-imaging study showing that division of a GFR α 1⁺ A_s cell generates, in most cases, an A_{pr} (Hara et al., 2014), the fact that most X cells are A_s (Figure 1I) motivated us to question whether X cells preferentially transit to a Plvap⁻ state following division. To address this hypothesis, we analyzed the fate of X cells that were in S phase, identified as GFP⁺/BrdU⁺ cells following simultaneous injection of 4OH-tamoxifen and bromodeoxyuridine (BrdU) (Figures S4H–S4K). We found that about 2/3 of GFP⁺/BrdU⁺ cells gave rise to one Plvap⁻ A_{pr} in 2 days. Subsequently, they followed highly variable fates including reacquisition of Plvap expression, syncytial fragmentation, as well as additional cell division and further differentiation. These findings substantiate a process of interconversion between Plvap⁺ and Plvap⁻ states.

Slow cycling of Plvap⁺ cells is locked with the seminiferous epithelial cycle

Next, we analyzed the cell-cycle status of X, Y, and Z cells in homeostasis. Short-term EdU incorporation assay showed that the proliferation rate was the lowest in X, becoming successively higher in Y and Z fractions (Figures 4A and S4L). Then, following continuous BrdU administration, we found that all X, Y, and Z cells were labeled within 9 days, indicating that dormant GFR α 1⁺ cells are absent or extremely rare (Figures 4B and S4M). Interestingly, the percentage of BrdU⁺ cells within the X cell compartment increased in an approximately linear manner, reaching ~100% by day 9 (Figures 4B and S4M). Since the variable timing of consecutive divisions would give rise to a nonlinear accumulation of BrdU⁺ cells, the observed linear dependence indicated that all X cells experience precisely one cell cycle (entry into S phase) during this period (Blanpain and Simons, 2013). To further characterize their cell cycle, mice were then pulsed sequentially with BrdU and EdU with variable time intervals (Figure 4C). The highest coincidence of BrdU and EdU label in X cells was observed at the 9-day time interval, consistent with a regular, or periodic, pattern of cell division with a period of 9 days. The minority population of BrdU⁺/EdU⁺ cells observed at shorter time intervals agreed with the transition into the X fraction from faster-cycling Y and Z cells.

Notably, the 9-day cell-cycle time coincided with the duration of the seminiferous epithelial cycle, the temporally periodic progression of spermatogenesis over a segment of the seminiferous tubules (Oakberg, 1956). In mice, this cycle shows a 9-day (more precisely, 8.6-day) periodicity and is divided into stages I–XII based on the local associations of differentiating cell types (Russell, 1990). The phase of the seminiferous epithelial cycle varies

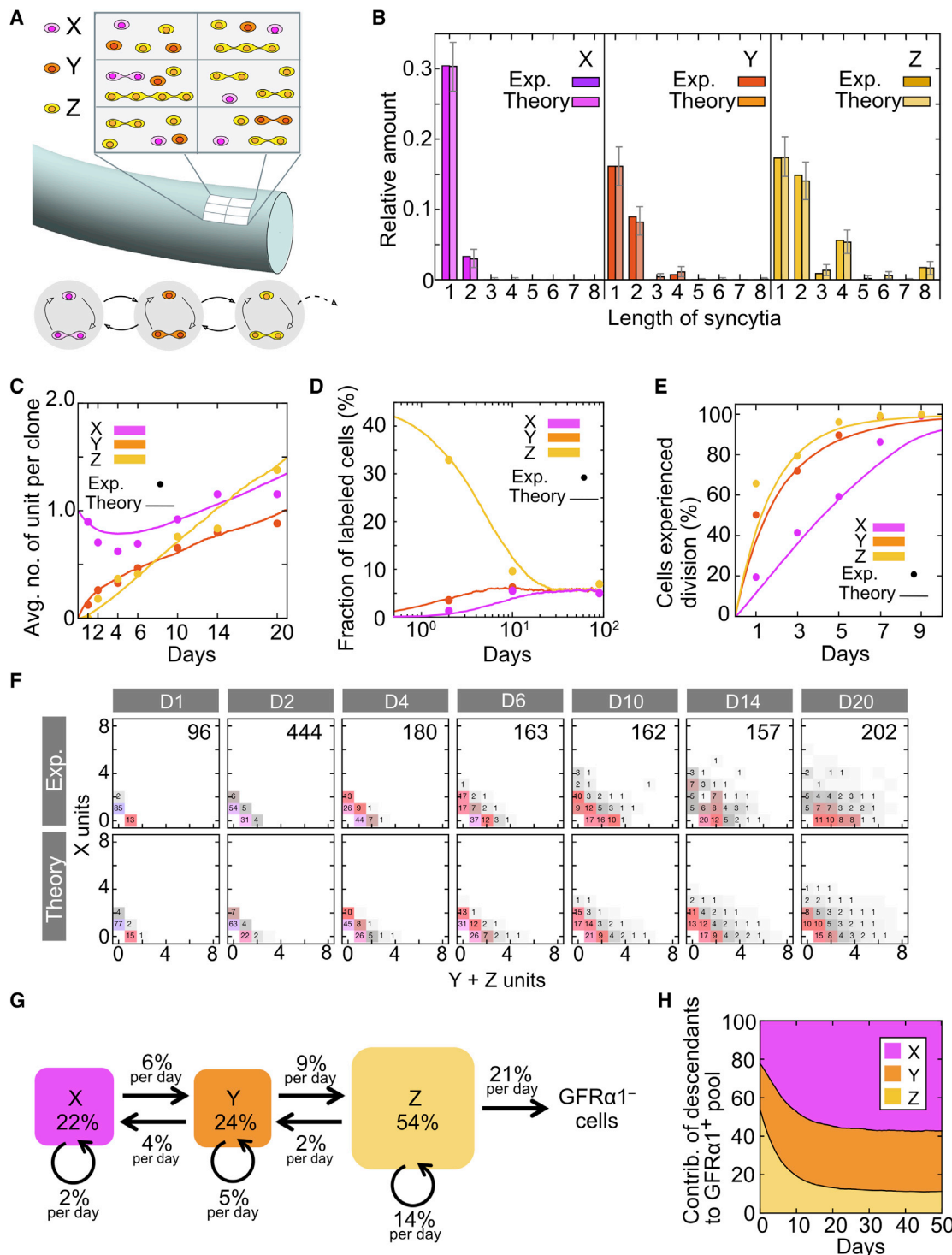


Figure 5. Biophysical model-based analysis of SSC dynamics

(A) Representation of the seminiferous tubule as a regular cylindrical lattice, with each domain harboring one X unit and an arbitrary number of Y and Z units, as a result of stochastic fate selection as shown (see [Figures S5A–S5C](#); [Data S2](#) for details).

(B–F) From a fit to the steady-state syncytial composition and the time-dependent average clone content, the model captures and predicts the observed behaviors of X, Y, and Z cells. These include (B) the syncytial composition in homeostasis (shown in comparison with the day 20 values; see [Figure 3G](#)), (C) kinetics of average clone composition in syncytial units, (D) fate of Sox3-labeled cells ([Figure 3K](#); induction efficiency of the Z fraction at day 0 was set to 45%), (E) cell

(legend continued on next page)

over the lengths of the tubules (Perey et al., 1961), so that the influence of the cycle is effectively averaged by observing tubules over a length of several centimeters, as applied in our standard analysis. In questioning the relationship between the cell cycle of X cells and the seminiferous epithelial cycle, we found that the number of X cells remained approximately constant, while those of Y and Z cells showed variabilities correlating with the phase of the cycle (Figure 4D). Indeed, an EdU incorporation assay revealed that X cells undergo S phase exclusively within a narrow time window between stages XI and I; Y and Z cells showed similar synchronicity, with their more frequent cell divisions broadening the S-phase time windows (Figure 4E).

The synchrony of X cell division with the seminiferous epithelial cycle provided an opportunity to determine the cell division rate of Y and Z cells: with an X cell-cycle length of 8.6 days, and 11.4% of X cells in S phase on average (Figure 4A), we could estimate their S phase length to be around 24 h (11.4% of 8.6 days). This result was in excellent agreement with an estimate in rats based on ³H-thymidine incorporation that indicated an S phase length of 24 h across the A_s, A_{pr} and A_{ai} population (Huckins, 1971c), suggesting that Y and Z cells in mouse may also have the same S phase length. Based on this reasoning, from the observed rate of short-term EdU incorporation, we estimated the average cell-cycle periods of Y and Z cells to be around 5 and 3 days, respectively (Data S2). Plvap⁺ (X) cells may constitute the mouse counterpart of the slow-cycling fraction of spermatogonia identified by Huckins in rats (showing 13-day cycle of seminiferous epithelium), which retained ³H-thymidine label for 13–19 days, but not longer (Huckins, 1971a).

A minimal model predicts quantitatively the homeostatic dynamics of X, Y, and Z cells

To gain deeper insight into the dynamics and fate behavior of SSCs during homeostasis, we then questioned whether the wide range of clonal-fate data and proliferation kinetics could be captured within the framework of a minimal theoretical model. Building upon a previous modeling scheme that sought to define the homeostatic dynamics of the GFR α 1⁺ population when approximated as a single equipotent compartment (Hara et al., 2014; Klein et al., 2010), we developed a refined model that took into account explicitly the apparent hierarchical organization and reversible transition of the X, Y, and Z cell fractions (Figures 5A and S5A–S5C; Data S2 for further details of the model). To enforce the observed uniform density dependence of X (Figure 4D), seminiferous tubules were represented as a cylindrical lattice with each site harboring either a single A_s, A_{pr}, or A_{ai} (defined as a “unit,” hereafter) of X cells (Figures 5A and S5A). Then, cells in X, Y, and Z fractions were allowed to undergo incomplete cell division, syncytial fragmentation, or state transition leading to differentiation (X-to-Y, Y-to-Z, and Z-to-GFR α 1[−]) or reversion (Y-to-X and Z-to-Y), in a stochastic (i.e., probabilistic) manner at defined rates (Figures S5B and S5C). To develop

a minimal model capturing the core dynamics of SSC homeostasis, the contribution of the GFR α 1[−] compartment was not considered, based on their negligible, if not zero, contribution to homeostasis (Hara et al., 2014). Consistent with this, Ngn3⁺ cells, which include essentially the entirety of GFR α 1[−] A_{undiff} and some GFR α 1⁺/Ngn3⁺ cells, make very low contributions to homeostasis (Figure 2F; Nakagawa et al., 2007), while GFR α 1[−]/Ngn3[−] A_{undiff} are extremely rare (about 0.1%). Similarly, other possible paths of state transitioning (e.g., direct X-to-Z or Z-to-X transitions), which were not motivated by experimental observations, were not included.

Based on experimental observations (Figure 4), X cell divisions were entrained with the seminiferous epithelial cycle with a period of 9 days; for simplicity, Y and Z cells were set to divide stochastically with the rates of once per 5 and 3 days on average, respectively (Figure S5B). Similarly, reflecting the experimental observations (Figures S4H–S4K), the division of X cells was coupled with a transition to the Y cell state whenever compatible with local density constraints (Figure S5C). Moreover, based on observations made in a previous intravital live-imaging study, GFR α 1⁺ cells were not allowed to undergo cell death (Hara et al., 2014). In this framework, the turnover of X, Y, and Z cells established a homeostatic steady state on the seminiferous tubules comprising either A_s or different lengths of syncytia (A_{pr} or A_{ai}), while continuously giving rise to differentiating, GFR α 1[−] cells.

From a fit of the model parameters to tissue average measures, including the size and morphological compositions of the X, Y, and Z fractions (Figure 3G), and the average clone content after pulse labeling of Plvap⁺ cells (Figure 3F), we found that the model could predict quantitatively a broad range of behaviors for all three compartments (Data S2). These included the intricate kinetics of clone size (e.g., the number of constituent cells) and composition (i.e., their transcriptional sub-states and morphology) after pulse labeling of X cells (Figures 5C, 5F, S5D, S5E, and S5G–S5I), the population-level kinetics of Sox3-induced cells (Figures 3K and 5D), and the kinetics of BrdU⁺ accumulation across all three compartments (Figures 4B, 5E, and S5F).

Such a predictive capacity provided confidence in the integrity of the modeling scheme and its underlying assumptions. In particular, these results suggested that GFR α 1⁺ cells select their fate (incomplete division, syncytial fragmentation, or transition to another state) based on the same probabilistic rules that depend only on their current transcriptional and morphological state, irrespective of their history. Further, using the measured and fitted parameter sets, this model provided a quantitative view of the cell flux dynamics within the SSC compartment (Figure 5G).

DISCUSSION

To understand the population dynamics of cells supporting the long-term homeostasis of mouse spermatogenesis, we identified subpopulations of GFR α 1⁺ A_{undiff} based on the expression

division kinetics during continual BrdU labeling (Figure 4B), and (F) bivariate clone size distributions of Plvap⁺ (X) versus Plvap[−] (Y+Z) compartments (with indicated number of analyzed clones from experiment; see Figures S5G–S5I for other marker gene combinations).

(G) Schematic showing the flux of cells between compartments based on the model simulation. Fluxes (arrows) and compartment sizes (rounded square) are given as the percentage of the entire GFR α 1⁺ cell population per day.

(H) Model-based kinetics of the fractions of the progenies of cells that were in X, Y, or Z fractions at day 0, which comprise the entire GFR α 1⁺ population.

Cell Reports

Article



of *Plvap* and *Sox3* and conducted quantitative fate analyses of these cells in unperturbed adult testes using pulse-labeling combined with mathematical modeling. We found that, while self-renewing potential is shared over the entirety of A_{undiff} , tissue maintenance depends almost entirely on an ensemble of heterogeneous cell states (termed X, Y, and Z) within the $GFR\alpha 1^+$ compartment, with $GFR\alpha 1^-$ (*Ngn3*⁺) cells rarely contributing to homeostasis. Within the $GFR\alpha 1^+$ compartment, this heterogeneous cell composition is maintained stably and robustly through continual interconversion between X, Y, and Z states that occur in a stochastic (probabilistic) and reversible fashion. In this scheme, cell states are organized in a hierarchical relationship in which X cells experience a bias toward renewal, while Z cells are primed for differentiation and loss from the self-renewing pool. However, through reversion between states (Y-to-X and Z-to-Y transitions), which occur at rates comparable to forward transitions (X-to-Y and Y-to-Z), cells are able to reassign their fate bias and contribute to long-term homeostasis (Figure 5G). Significantly, X cells that result from reversion from the Y and Z compartments have the same renewal potential and follow the same stochastic fate behavior, as “existing” X cells. It therefore follows that the transition from self-renewal to differentiation is not a direct process of “commitment” but proceeds indirectly through distinct intermediate “primed state(s).”

In this framework, X, Y, and Z cells have a differing survival probability over the short term, with X showing the highest renewal potential. However, once a clone extends over the three fractions of $GFR\alpha 1^+$ cells in a representative manner, its subsequent long-term evolution becomes independent of the original cell state. As a consequence, each of the X, Y, and Z fractions makes a significant contribution to the $GFR\alpha 1^+$ pool over the long term (estimated at 58%, 31%, and 11%, respectively, according to the results of the model simulation) (Figure 5H). Such behavior explains both the large difference in frequency of patch formation observed experimentally over the long term (Figure 2F) and the indistinguishability of the size distributions and X, Y, and Z cell content of individual clonal patches between those derived from different subsets of $GFR\alpha 1^+$ cells (Figure 2G). Further, more downstream $GFR\alpha 1^-$ (*Ngn3*⁺) A_{undiff} also make a non-zero contribution to long-term homeostasis, forming clonal patches indistinguishable from those derived from $GFR\alpha 1^+$ cells, despite their rarity. Therefore, this scheme can be extended to the $GFR\alpha 1^-$ states, although their contribution to homeostasis is too small to be quantified reliably within the current modeling framework.

We propose that subpopulations of A_{undiff} broadly harbor stem cell *potential*, founded on the interconversion between their different states; each state shows a differing probability to contribute to long-term self-renewal depending on its position within the stem cell hierarchy and the tissue context. Such SSC dynamics, showing both hierarchical and equipotent properties, may reconcile conflicting hypotheses proposed for the identity and function of mouse SSCs during homeostasis (de Rooij, 2017; Lord and Oatley, 2017; Mäkelä and Hobbs, 2019; Yoshida, 2019). In homeostasis, cells at the top of the hierarchy (viz. the X state) have a higher survival probability than those lower in the hierarchy (Y, Z, and, more substantially, $GFR\alpha 1^-$ cells). However, once the progenies of cells of different states have spread representatively over the heterogeneous stem cell

pool, they subsequently follow collectively the same stochastic fate behavior, independent of the original state. Over the long term, the molecularly heterogeneous population of SSCs therefore functions as a single “equipotent” pool.

This framework may also explain the context-dependent cell-fate plasticity of $GFR\alpha 1^-$ A_{undiff} (Nakagawa et al., 2007, 2010). While retaining self-renewing potential, on transition to a $GFR\alpha 1^-$ state of A_{undiff} , cells also become susceptible to irreversible differentiation promoted by retinoic acid (RA) signaling mediated by the expression of *RAR γ* , a RA receptor (Gely-Pernot et al., 2012; Ikami et al., 2015). During homeostasis, in synchrony with the seminiferous epithelial cycle, transitioning from $GFR\alpha 1^+$ /*RAR γ* [−] to $GFR\alpha 1^-$ /*RAR γ* ⁺ states occurs around stages IV–V, which is followed shortly after by an increase of tissue RA concentration in stages VII–VIII (Endo et al., 2017; Hogarth et al., 2015). As a consequence, most $GFR\alpha 1^-$ cells transition into differentiating spermatogonia, without reverting to a $GFR\alpha 1^+$ state during homeostasis. However, in a regenerative context, when the open niche is much less crowded, the supremacy of the $GFR\alpha 1^+$ cell population or temporal orchestration of seminiferous epithelial cycle may be compromised. In such a situation, reversion from $GFR\alpha 1^-$ states to $GFR\alpha 1^+$ states may become more prevalent, raising significantly the probability for $GFR\alpha 1^-$ A_{undiff} to contribute to long-term self-renewal.

These findings motivated us to question the molecular pathways by which cells transition reversibly between X, Y, and Z states, by analyzing published scRNA-seq data (La et al., 2018). Although the X, Y, and Z cell states are defined and studied based only on the expression of few genes (e.g., *GFR $\alpha 1$* , *Plvap*, and *Sox3*) using immunofluorescence and transgenic reporter models, we found considerable consistencies between these states and the results of unbiased clustering of scRNA-seq data (Figures 1D and S1H–S1L). We could annotate cell clusters showing the X and Z state identity, based on the expression profiles of *GFR $\alpha 1$* , *Plvap*, and *Sox3*, as well as other genes showing positive or negative correlations with each other (Figures 1D and S1H–S1L). Similarly, cells showing intermediate expression of X and Z state-associated genes were annotated to be at the “Y” state, which were located between X and Z clusters on the UMAP. Interestingly, these cells appeared not to comprise a discrete single population, but to be heterogeneous, spanning two clusters (designated as Y1 and Y2) (Figures S1I–S1K). Intriguingly, our pseudotime analysis suggested two distinct trajectories; one transitions “linearly” along $X \rightarrow Y1 \rightarrow Z \rightarrow \text{Ngn3}^+$ differentiating cells, and the other “circles” around $X \rightarrow Y1 \rightarrow Z \rightarrow Y2 \rightarrow X$ (Figure S1L). This result implies that Y1 and Y2 might represent distinct transitional states mediating differentiating (X-to-Z) and reversing (Z-to-X) routes, respectively, showing different landscapes at the molecular level (Figures S1M–S1N; Table S3). However, further in-depth single-cell analyses that trace the dynamics of targeted cell populations will be required to confirm the observed molecular heterogeneity and its significance for bidirectional transitioning between SSC states.

Using an *in vitro* assay, we also found that genes correlated with X and Z states are up- and downregulated, respectively, by FGFs (i.e., *FGF2* and *FGF5*) and *GDNF*, suggesting that the transition between X, Y, and Z states may be regulated by the

strengths of these niche-derived factors (Figures S2H–S2M) (Kitadate et al., 2019; Meng et al., 2000). These findings are resonant with a recently proposed feedback mechanism of homeostatic SSC density regulation, in which SSCs effectively “sense” their local density through the reception and consumption of niche factors, adjusting their fate bias in response: when exposed to high and low concentration of these factors, SSCs will be inclined for renewal and differentiation, respectively (Jörg et al., 2021; Kitadate et al., 2019). Based on these insights, future studies will explore the molecular regulatory programs that mediate SSC state transitions and fate behavior.

Regarding substate heterogeneity of the SSC compartment, this study also uncovered a striking correlation between short-term renewal potential, and cell-cycle length and timing. Previously, models of stem cell homeostasis have placed emphasis on stem cell hierarchies in which a small and discrete population of slow-cycling stem cells persist over the long term, while maintaining a downstream faster-cycling population of progenitors with only limited renewal potential. Indeed, experimental evidence in support of this paradigm has accumulated in the context of hematopoiesis (Boyer et al., 2011; Busch et al., 2015; Cheshier et al., 1999). However, in the context of mouse spermatogenesis, we found that slow-cycling SSCs do not by themselves constitute the persisting population, but SSCs are heterogeneous transiting stochastically and reversibly between a slow-cycling, renewal-biased, state ($GFR\alpha 1^+/Plvap^+$ or X), and a faster-cycling, differentiation-primed, state ($GFR\alpha 1^+/Sox3^+$ or Z). Unexpectedly, we discovered that SSCs in the $Plvap^+$ (X) state divide regularly, in perfect synchrony with the seminiferous epithelial cycle. This singular behavior suggests that the periodic seminiferous epithelial cycle may entrain the division timing of the $Plvap^+$ population, establishing a tight connection between SSC activity and the tissue-level control of sperm production and maturation. Of note, GDNF expression in Sertoli cells shows a concomitant pattern with the division timing of $Plvap^+$ SSCs in stages XI–IV, suggesting that GDNF may play a key role in regulating their division periodicity (Figure 4) (Sato et al., 2011; Sharma and Braun, 2018; Tokue et al., 2017).

Based on the mathematical modeling scheme, quantitative analysis of the inferred SSC dynamics can effectively reduce the net number of cell divisions in the long-term self-renewing pool by around 1.5-fold compared to that expected for systems in which all stem cells divide at the same average rate (Data S2). This reduction may provide a good compromise in mitigating the risk of acquiring harmful *de novo* mutations, while maintaining the effective stem cell density. The model suggests that SSCs experience about 60 divisions per year on average (Data S2). While this number may be small enough to safely maintain genome integrity in short-lived animals such as mice, long-lived animals like humans might call for an additional mechanism to further reduce the mitotic load during their decades-long reproduction period. In this regard, recent scRNA-seq studies of human testes have revealed a population of $GFR\alpha 1^+$ spermatogonia. However, unlike mice, these cells do not lie at the most undifferentiated end, but, rather, the apex of the differentiation hierarchy appears to be occupied by a small discrete population of $GFR\alpha 1^-$ cells that are transcriptionally distinct from the majority of $GFR\alpha 1^-$ spermatogonia located downstream of the $GFR\alpha 1^+$ population (Guo et al., 2018). While the dynamical

behavior of human spermatogonial populations remain to be elucidated, an interesting hypothesis is that such $GFR\alpha 1^-$ cells at the apex act as a dormant reserve population, supplying cells infrequently to a downstream cycling SSC compartment and effectively decreasing the overall mitotic load, as implicated classically for A_{dark} spermatogonia (Fayomi and Orwig, 2018).

Finally, the inferred stochastic interconversion between states biased for self-renewal and primed for differentiation is resonant with reports in the mouse small intestine based on *in vivo* time-lapse imaging (Ritsma et al., 2014). However, such behavior could be maintained through the anatomical heterogeneity of the stem cell niche at the crypt base, reflecting the glandular organization of the intestinal epithelium. Stem cells positioned close to the niche border are more likely to become displaced from the niche and differentiate, while cells at the crypt base experience a positional bias to remain within the niche. By contrast, in testicular seminiferous tubules, SSC substates experience no obvious sustained positional bias, while SSC density is higher near the interstitium, SSCs lie scattered among their differentiating progenies, and migrate actively over the largely homogeneous “open niche” microenvironment (Hara et al., 2014; Yoshida, 2018; Yoshida et al., 2007b). Such a multistate SSC dynamics may serve as paradigm to define stem cell organization in other tissue types supported by an open niche.

Limitations of study

To capture dynamical relationships between X, Y, Z, and $GFR\alpha 1^-$ fractions, our mathematical model has been structured according to the sequence of states, X–Y–Z– $GFR\alpha 1^-$, based on the chronological ordering of the expansion of labeled cells following induction of X cells, and the arrangement of cell clusters in the dimension reduction space in the scRNA-seq analysis. Although additional processes involving the skipping of some states (e.g., X-to-Z transition) cannot be excluded, the net effect of such transitions is already included implicitly through a sequence of existing channels (e.g., X-to-Y followed by Y-to-Z). Similarly, X, Y, and Z compartments are all considered to be homogeneous, with cells selecting their fate stochastically depending only on their current state. However, the effects of transcriptional heterogeneities within individual cell substates cannot be excluded.

Given that the current mathematical model can already capture quantitatively the broad range of multi-dimensional data obtained by experiments at the current resolution, the addition of very rare processes (e.g., reversion from $GFR\alpha 1^-$ cells to $GFR\alpha 1^+$ cells) or populations (e.g., $GFR\alpha 1^-/Ngn3^- A_{undiff}$), as well as further cell heterogeneity within the X, Y, or Z compartments would not lead to an increase of its explanatory power. Future analyses of SSC states and their transition kinetics with higher resolution may motivate the development models with higher complexity, which could further deepen our understanding of heterogeneous SSC dynamics.

STAR★METHODS

Detailed methods are provided in the online version of this paper and include the following:

- KEY RESOURCES TABLE

Cell Reports

Article



- **RESOURCE AVAILABILITY**
 - Lead contact
 - Materials availability
 - Data and code availability
- **EXPERIMENTAL MODEL AND SUBJECT DETAILS**
 - Animals
- **METHOD DETAILS**
 - Generation of Plvav^{CreERT2} and Sox3-CreER^{T2} alleles
 - Pulse-labeling experiments using CreER-loxP system
 - S-phase labeling with BrdU and/or EdU
 - Dual-pulse labeling experiment with BrdU and 4OH-tamoxifen
 - Antibodies used for immunostaining and FACS
 - Immunofluorescence staining of testicular sections
 - Whole-mount immunofluorescence
 - Flow-cytometry and cell sorting
 - Quantitative RT-PCR of sorted cell fractions
 - Transplantation
 - Single-cell multiplexed qRT-PCR
 - Reanalysis of single-cell RNA-seq data
 - Dimension reduction and clustering
 - Annotating cell clusters into five cell states
 - Pseudotime analysis
 - Effect of FGFs and GDNF on cultured spermatogonia
 - Statistical analysis

SUPPLEMENTAL INFORMATION

Supplemental information can be found online at <https://doi.org/10.1016/j.celrep.2021.109875>.

ACKNOWLEDGMENTS

We thank J. Miyazaki, P. Chambon, and N.G. Copeland for providing *CAG-AT-EGFP* mice, *CreERT2* construct, and materials for BAC recombination, respectively. We are grateful to Y. Kitadate, H. Mizuguchi, Y. Nakamura, T. Sato, K. Hirano, S. Hira, K. Yoshido, G. Palfalvi, T. Ogawa, and T. Sugiyama for useful discussions and encouragement, C. Nishimoto for technical assistance, S. Hira for communicating a result of cell-fate analysis, Y. Kuboki for secretarial assistance, and N. Yoshida for help in calculation. We thank the NIBB Core Research Facilities for single-cell multiplexed qRT-PCR and the Model Animal Research Facility of NIBB Bioresource Center and Laboratory of Regenerative Animal Experiment of Kyoto University for animal care. This work is funded by MEXT and JSPS (Grant-in-Aid for Scientific Research KAKENHI JP23770245, JP25711014, and JP17K07424 to T. Nakagawa; JP16H02507, JP25114004, and JP18H05551 to S.Y.; and JP18H03998 to T. Nagasawa); AMED (JP17gm1110005h0001 to S.Y.); the Royal Society E.P. Abraham Research Professorship (RP/R1/180165 to B.D.S.); Wellcome Trust (098357/Z/12/Z and 219478/Z/19/Z to B.D.S.); MRC-AMED Regenerative Medicine and Stem Cell Research Initiative (MR/V005405/1 to B.D.S. and JP20bm0704057h0001 to S.Y.); and Cooperative Research Program (Joint Usage/Research Center program) of Institute for Frontier Life and Medical Sciences, Kyoto University to T. Nagasawa. S.H. acknowledges supports from Human Frontier Science Program (LT00092/2016-L) and National Research Foundation of Korea (Basic Science Research Program; NRF-2014R1A6A3A01005675).

AUTHOR CONTRIBUTIONS

T. Nakagawa and T. Nagasawa designed the initial research framework. T. Nakagawa, T. Nagasawa, B.D.S., and S.Y. organized and conceptualized this collaborative study. T. Nakagawa performed the screening experiments using single-cell multiplexed qRT-PCR, cell-sorting, and *in vivo* experiments. T. Na-

kagawa and Y.O. developed a critical cell-sorting strategy. S.H., T.I., T. Nakagawa, B.D.S., and S.Y. analyzed the published scRNA-seq data. T. Nakagawa, K.N., and M.F. performed important immunostaining for this article. T. Nakagawa, H.W., G.K., S.M., and S.T. generated genetically modified mice. D.J.J. and B.D.S. performed modeling analyses. T. Nakagawa, D.J.J., S.H., B.D.S., T. Nagasawa, and S.Y. wrote the manuscript with input from all other authors.

DECLARATION OF INTERESTS

The authors declare no competing interests.

Received: September 22, 2020

Revised: August 17, 2021

Accepted: September 29, 2021

Published: October 19, 2021

SUPPORTING CITATIONS

The following references appear in the Supplemental information: Gillespie, 1977; Hansen et al., 2019; Jörg, 2017.

REFERENCES

- Aloisio, G.M., Nakada, Y., Saatioglu, H.D., Peña, C.G., Baker, M.D., Tarnawa, E.D., Mukherjee, J., Manjunath, H., Bugde, A., Sengupta, A.L., et al. (2014). PAX7 expression defines germline stem cells in the adult testis. *J. Clin. Invest.* *124*, 3929–3944.
- Barker, N., van Es, J.H., Kuipers, J., Kujala, P., van den Born, M., Cozijnsen, M., Haegebarth, A., Korving, J., Begthel, H., Peters, P.J., and Clevers, H. (2007). Identification of stem cells in small intestine and colon by marker gene *Lgr5*. *Nature* *449*, 1003–1007.
- Blanpain, C., and Simons, B.D. (2013). Unravelling stem cell dynamics by lineage tracing. *Nat. Rev. Mol. Cell Biol.* *14*, 489–502.
- Blondel, V.D., Guillaume, J.-L., Lambiotte, R., and Lefebvre, E. (2008). Fast unfolding of communities in large networks. *J. Stat. Mech. Theory Exp.* *2008*, P10008.
- Boyer, S.W., Schroeder, A.V., Smith-Berdan, S., and Forsberg, E.C. (2011). All hematopoietic cells develop from hematopoietic stem cells through Flk2/Flt3-positive progenitor cells. *Cell Stem Cell* *9*, 64–73.
- Brinster, R.L., and Zimmermann, J.W. (1994). Spermatogenesis following male germ-cell transplantation. *Proc. Natl. Acad. Sci. USA* *91*, 11298–11302.
- Buczacki, S.J., Zecchini, H.I., Nicholson, A.M., Russell, R., Vermeulen, L., Kemp, R., and Winton, D.J. (2013). Intestinal label-retaining cells are secretory precursors expressing *Lgr5*. *Nature* *495*, 65–69.
- Busch, K., Klapproth, K., Barile, M., Flossdorf, M., Holland-Letz, T., Schlenner, S.M., Reth, M., Höfer, T., and Rodewald, H.R. (2015). Fundamental properties of unperturbed haematopoiesis from stem cells *in vivo*. *Nature* *518*, 542–546.
- Carrieri, C., Comazzetto, S., Grover, A., Morgan, M., Bunes, A., Nerlov, C., and O'Carroll, D. (2017). A transit-amplifying population underpins the efficient regenerative capacity of the testis. *J. Exp. Med.* *214*, 1631–1641.
- Chan, F., Oatley, M.J., Kaucher, A.V., Yang, Q.E., Bieberich, C.J., Shashikant, C.S., and Oatley, J.M. (2014). Functional and molecular features of the Id4+ germline stem cell population in mouse testes. *Genes Dev.* *28*, 1351–1362.
- Cheshier, S.H., Morrison, S.J., Liao, X., and Weissman, I.L. (1999). *In vivo* proliferation and cell cycle kinetics of long-term self-renewing hematopoietic stem cells. *Proc. Natl. Acad. Sci. USA* *96*, 3120–3125.
- Chiarini-García, H., Hornick, J.R., Griswold, M.D., and Russell, L.D. (2001). Distribution of type A spermatogonia in the mouse is not random. *Biol. Reprod.* *65*, 1179–1185.
- Cotsarelis, G., Sun, T.T., and Lavker, R.M. (1990). Label-retaining cells reside in the bulge area of pilosebaceous unit: implications for follicular stem cells, hair cycle, and skin carcinogenesis. *Cell* *61*, 1329–1337.

- de Rooij, D.G. (2017). The nature and dynamics of spermatogonial stem cells. *Development* **144**, 3022–3030.
- de Sousa E Melo, F., and de Sauvage, F.J. (2019). Cellular Plasticity in Intestinal Homeostasis and Disease. *Cell Stem Cell* **24**, 54–64.
- Endo, T., Freinkman, E., de Rooij, D.G., and Page, D.C. (2017). Periodic production of retinoic acid by meiotic and somatic cells coordinates four transitions in mouse spermatogenesis. *Proc. Natl. Acad. Sci. USA* **114**, E10132–E10141.
- Farley, F.W., Soriano, P., Steffen, L.S., and Dymecki, S.M. (2000). Widespread recombinase expression using FLP_{eR} (flipper) mice. *Genesis* **28**, 106–110.
- Fayomi, A.P., and Orwig, K.E. (2018). Spermatogonial stem cells and spermatogenesis in mice, monkeys and men. *Stem Cell Res. (Amst.)* **29**, 207–214.
- Feil, R., Wagner, J., Metzger, D., and Chambon, P. (1997). Regulation of Cre recombinase activity by mutated estrogen receptor ligand-binding domains. *Biochem. Biophys. Res. Commun.* **237**, 752–757.
- Fuller, M.T., and Spradling, A.C. (2007). Male and female *Drosophila* germline stem cells: two versions of immortality. *Science* **316**, 402–404.
- Garbuzov, A., Pech, M.F., Hasegawa, K., Sukhwani, M., Zhang, R.J., Orwig, K.E., and Artandi, S.E. (2018). Purification of GFR α 1+ and GFR α 1- Spermatogonial Stem Cells Reveals a Niche-Dependent Mechanism for Fate Determination. *Stem Cell Reports* **10**, 553–567.
- Gely-Pernot, A., Raverdeau, M., Célèbi, C., Dennefeld, C., Feret, B., Klopfenstein, M., Yoshida, S., Ghyselinck, N.B., and Mark, M. (2012). Spermatogonia differentiation requires retinoic acid receptor γ . *Endocrinology* **153**, 438–449.
- Gillespie, D.T. (1977). Exact stochastic simulation of coupled chemical reactions. *J. Phys. Chem. A* **81**, 2340–2361.
- Guo, J., Grow, E.J., Mlcochova, H., Maher, G.J., Lindskog, C., Nie, X., Guo, Y., Takei, Y., Yun, J., Cai, L., et al. (2018). The adult human testis transcriptional cell atlas. *Cell Res.* **28**, 1141–1157.
- Hansen, N., Akimoto, Y., and Baudis, P. (2019). CMA-ES/pycma on Github. Zenodo.
- Hara, K., Nakagawa, T., Enomoto, H., Suzuki, M., Yamamoto, M., Simons, B.D., and Yoshida, S. (2014). Mouse spermatogenic stem cells continually interconvert between equipotent singly isolated and syncytial states. *Cell Stem Cell* **14**, 658–672.
- Hogan, B.L., Barkauskas, C.E., Chapman, H.A., Epstein, J.A., Jain, R., Hsia, C.C., Niklason, L., Calle, E., Le, A., Randell, S.H., et al. (2014). Repair and regeneration of the respiratory system: complexity, plasticity, and mechanisms of lung stem cell function. *Cell Stem Cell* **15**, 123–138.
- Hogarth, C.A., Arnold, S., Kent, T., Mitchell, D., Isoherranen, N., and Griswold, M.D. (2015). Processive pulses of retinoic acid propel asynchronous and continuous murine sperm production. *Biol. Reprod.* **92**, 37.
- Huckins, C. (1971a). The spermatogonial stem cell population in adult rats. 3. Evidence for a long-cycling population. *Cell Tissue Kinet.* **4**, 335–349.
- Huckins, C. (1971b). The spermatogonial stem cell population in adult rats. I. Their morphology, proliferation and maturation. *Anat. Rec.* **169**, 533–557.
- Huckins, C. (1971c). The spermatogonial stem cell population in adult rats. II. A radioautographic analysis of their cell cycle properties. *Cell Tissue Kinet.* **4**, 313–334.
- Ikami, K., Tokue, M., Sugimoto, R., Noda, C., Kobayashi, S., Hara, K., and Yoshida, S. (2015). Hierarchical differentiation competence in response to retinoic acid ensures stem cell maintenance during mouse spermatogenesis. *Development* **142**, 1582–1592.
- Imuta, Y., Kiyonari, H., Jang, C.W., Behringer, R.R., and Sasaki, H. (2013). Generation of knock-in mice that express nuclear enhanced green fluorescent protein and tamoxifen-inducible Cre recombinase in the notochord from Foxa2 and T loci. *Genesis* **51**, 210–218.
- Jörg, D.J. (2017). Stochastic Kuramoto oscillators with discrete phase states. *Phys. Rev. E* **96**, 032201.
- Jörg, D.J., Kitadate, Y., Yoshida, S., and Simons, B.D. (2021). Stem Cell Populations as Self-Renewing Many-Particle Systems. *Annu. Rev. Condens. Matter Phys.* **12**, 135–153.
- Kanatsu-Shinohara, M., Ogonuki, N., Inoue, K., Miki, H., Ogura, A., Toyokuni, S., and Shinohara, T. (2003). Long-term proliferation in culture and germline transmission of mouse male germline stem cells. *Biol. Reprod.* **69**, 612–616.
- Kawamoto, S., Niwa, H., Tashiro, F., Sano, S., Kondoh, G., Takeda, J., Tabayashi, K., and Miyazaki, J. (2000). A novel reporter mouse strain that expresses enhanced green fluorescent protein upon Cre-mediated recombination. *FEBS Lett.* **470**, 263–268.
- Kitadate, Y., Jörg, D.J., Tokue, M., Maruyama, A., Ichikawa, R., Tsuchiya, S., Segi-Nishida, E., Nakagawa, T., Uchida, A., Kimura-Yoshida, C., et al. (2019). Competition for Mitogens Regulates Spermatogenic Stem Cell Homeostasis in an Open Niche. *Cell Stem Cell* **24**, 79–92.e6.
- Klein, A.M., Nakagawa, T., Ichikawa, R., Yoshida, S., and Simons, B.D. (2010). Mouse germ line stem cells undergo rapid and stochastic turnover. *Cell Stem Cell* **7**, 214–224.
- La, H.M., and Hobbs, R.M. (2019). Mechanisms regulating mammalian spermatogenesis and fertility recovery following germ cell depletion. *Cell. Mol. Life Sci.* **76**, 4071–4102.
- La, H.M., Mäkelä, J.A., Chan, A.L., Rossello, F.J., Nefzger, C.M., Legrand, J.M.D., De Seram, M., Polo, J.M., and Hobbs, R.M. (2018). Identification of dynamic undifferentiated cell states within the male germline. *Nat. Commun.* **9**, 2819.
- Lee, E.C., Yu, D., Martinez de Velasco, J., Tessarollo, L., Swing, D.A., Court, D.L., Jenkins, N.A., and Copeland, N.G. (2001). A highly efficient Escherichia coli-based chromosome engineering system adapted for recombinogenic targeting and subcloning of BAC DNA. *Genomics* **73**, 56–65.
- Lord, T., and Oatley, J.M. (2017). A revised A_{single} model to explain stem cell dynamics in the mouse male germline. *Reproduction* **154**, R55–R64.
- Lun, A.T., McCarthy, D.J., and Marioni, J.C. (2016). A step-by-step workflow for low-level analysis of single-cell RNA-seq data with Bioconductor. *F1000Res.* **5**, 2122.
- Mäkelä, J.A., and Hobbs, R.M. (2019). Molecular regulation of spermatogonial stem cell renewal and differentiation. *Reproduction* **158**, R169–R187.
- McCarthy, D.J., Campbell, K.R., Lun, A.T., and Wills, Q.F. (2017). Scater: pre-processing, quality control, normalization and visualization of single-cell RNA-seq data in R. *Bioinformatics* **33**, 1179–1186.
- Meng, X., Lindahl, M., Hyvönen, M.E., Parvinen, M., de Rooij, D.G., Hess, M.W., Raatikainen-Ahokas, A., Sainio, K., Rauvala, H., Lakso, M., et al. (2000). Regulation of cell fate decision of undifferentiated spermatogonia by GDNF. *Science* **287**, 1489–1493.
- Merrell, A.J., and Stanger, B.Z. (2016). Adult cell plasticity in vivo: de-differentiation and transdifferentiation are back in style. *Nat. Rev. Mol. Cell Biol.* **17**, 413–425.
- Nakagawa, T., Nabeshima, Y., and Yoshida, S. (2007). Functional identification of the actual and potential stem cell compartments in mouse spermatogenesis. *Dev. Cell* **12**, 195–206.
- Nakagawa, T., Sharma, M., Nabeshima, Y., Braun, R.E., and Yoshida, S. (2010). Functional hierarchy and reversibility within the murine spermatogenic stem cell compartment. *Science* **328**, 62–67.
- Nakamura, Y., Jörg, D.J., Kon, Y., Simons, B.D., and Yoshida, S. (2021). Transient suppression of transplanted spermatogonial stem cell differentiation restores fertility in mice. *Cell Stem Cell* **28**, 1443–1456.e7.
- Oakberg, E.F. (1956). A description of spermiogenesis in the mouse and its use in analysis of the cycle of the seminiferous epithelium and germ cell renewal. *Am. J. Anat.* **99**, 391–413.
- Ogawa, T., Aréchaga, J.M., Avarbock, M.R., and Brinster, R.L. (1997). Transplantation of testis germinal cells into mouse seminiferous tubules. *Int. J. Dev. Biol.* **41**, 111–122.
- Okabe, M., Ikawa, M., Kominami, K., Nakanishi, T., and Nishimune, Y. (1997). ‘Green mice’ as a source of ubiquitous green cells. *FEBS Lett.* **407**, 313–319.
- Perey, B., Clermont, Y., and Leblond, C.P. (1961). The wave of the seminiferous epithelium in the rat. *Am. J. Anat.* **108**, 47–77.

Cell Reports

Article



- Potten, C.S., Kovacs, L., and Hamilton, E. (1974). Continuous labelling studies on mouse skin and intestine. *Cell Tissue Kinet.* **7**, 271–283.
- Raverot, G., Weiss, J., Park, S.Y., Hurley, L., and Jameson, J.L. (2005). Sox3 expression in undifferentiated spermatogonia is required for the progression of spermatogenesis. *Dev. Biol.* **283**, 215–225.
- Ritsma, L., Ellenbroek, S.I.J., Zomer, A., Snippert, H.J., de Sauvage, F.J., Simons, B.D., Clevers, H., and van Rheenen, J. (2014). Intestinal crypt homeostasis revealed at single-stem-cell level by in vivo live imaging. *Nature* **507**, 362–365.
- Russell, L., Ettlin, R., Sinha Hikim, A., and Clegg, E. (1990). *Histological and Histopathological Evaluation of the Testis* (Cache River Press).
- Sada, A., Suzuki, A., Suzuki, H., and Saga, Y. (2009). The RNA-binding protein NANOS2 is required to maintain murine spermatogonial stem cells. *Science* **325**, 1394–1398.
- Sato, T., Aiyama, Y., Ishii-Inagaki, M., Hara, K., Tsunekawa, N., Harikae, K., Uemura-Kamata, M., Shinomura, M., Zhu, X.B., Maeda, S., et al. (2011). Cyclical and patch-like GDNF distribution along the basal surface of Sertoli cells in mouse and hamster testes. *PLoS ONE* **6**, e28367.
- Sharma, M., and Braun, R.E. (2018). Cyclical expression of GDNF is required for spermatogonial stem cell homeostasis. *Development* **145**, dev151555.
- Sharma, M., Srivastava, A., Fairfield, H.E., Bergstrom, D., Flynn, W.F., and Braun, R.E. (2019). Identification of EOMES-expressing spermatogonial stem cells and their regulation by PLZF. *eLife* **8**.
- Snippert, H.J., van der Flier, L.G., Sato, T., van Es, J.H., van den Born, M., Kroon-Veenboer, C., Barker, N., Klein, A.M., van Rheenen, J., Simons, B.D., and Clevers, H. (2010). Intestinal crypt homeostasis results from neutral competition between symmetrically dividing Lgr5 stem cells. *Cell* **143**, 134–144.
- Street, K., Risso, D., Fletcher, R.B., Das, D., Ngai, J., Yosef, N., Purdom, E., and Dudoit, S. (2018). Slingshot: cell lineage and pseudotime inference for single-cell transcriptomics. *BMC Genomics* **19**, 477.
- Stuart, T., Butler, A., Hoffman, P., Hafemeister, C., Papalexi, E., Mauck, W.M., 3rd, Hao, Y., Stoeckius, M., Smibert, P., and Satija, R. (2019). Comprehensive Integration of Single-Cell Data. *Cell* **177**, 1888–1902.e21.
- Suzuki, S., McCarrey, J.R., and Hermann, B.P. (2021). An mTORC1-dependent switch orchestrates the transition between mouse spermatogonial stem cells and clones of progenitor spermatogonia. *Cell Rep.* **34**, 108752.
- Tokue, M., Ikami, K., Mizuno, S., Takagi, C., Miyagi, A., Takada, R., Noda, C., Kitadate, Y., Hara, K., Mizuguchi, H., et al. (2017). SHISA6 Confers Resistance to Differentiation-Promoting Wnt/ β -Catenin Signaling in Mouse Spermatogenic Stem Cells. *Stem Cell Reports* **8**, 561–575.
- Uesaka, T., Jain, S., Yonemura, S., Uchiyama, Y., Milbrandt, J., and Enomoto, H. (2007). Conditional ablation of GFRalpha1 in postmigratory enteric neurons triggers unconventional neuronal death in the colon and causes a Hirschsprung's disease phenotype. *Development* **134**, 2171–2181.
- Watt, F.M., and Hogan, B.L. (2000). Out of Eden: stem cells and their niches. *Science* **287**, 1427–1430.
- Yoshida, S. (2018). Open niche regulation of mouse spermatogenic stem cells. *Dev. Growth Differ.* **60**, 542–552.
- Yoshida, S. (2019). Heterogeneous, dynamic, and stochastic nature of mammalian spermatogenic stem cells. *Curr. Top. Dev. Biol.* **135**, 245–285.
- Yoshida, S., Takakura, A., Ohbo, K., Abe, K., Wakabayashi, J., Yamamoto, M., Suda, T., and Nabeshima, Y. (2004). Neurogenin3 delineates the earliest stages of spermatogenesis in the mouse testis. *Dev. Biol.* **269**, 447–458.
- Yoshida, S., Sukeno, M., Nakagawa, T., Ohbo, K., Nagamatsu, G., Suda, T., and Nabeshima, Y. (2006). The first round of mouse spermatogenesis is a distinctive program that lacks the self-renewing spermatogonia stage. *Development* **133**, 1495–1505.
- Yoshida, S., Nabeshima, Y., and Nakagawa, T. (2007a). Stem cell heterogeneity: actual and potential stem cell compartments in mouse spermatogenesis. *Ann. N Y Acad. Sci.* **1120**, 47–58.
- Yoshida, S., Sukeno, M., and Nabeshima, Y. (2007b). A vasculature-associated niche for undifferentiated spermatogonia in the mouse testis. *Science* **317**, 1722–1726.
- Yoshinaga, K., Nishikawa, S., Ogawa, M., Hayashi, S., Kunisada, T., Fujimoto, T., and Nishikawa, S. (1991). Role of c-kit in mouse spermatogenesis: identification of spermatogonia as a specific site of c-kit expression and function. *Development* **113**, 689–699.
- Zhou, Q., Nie, R., Li, Y., Friel, P., Mitchell, D., Hess, R.A., Small, C., and Griswold, M.D. (2008). Expression of stimulated by retinoic acid gene 8 (Stra8) in spermatogenic cells induced by retinoic acid: an in vivo study in vitamin A-sufficient postnatal murine testes. *Biol. Reprod.* **79**, 35–42.

STAR★METHODS

KEY RESOURCES TABLE

Reagent or resource	Source	Identifier
Antibodies		
Rat anti-PLVAP	Biolegend	Cat#120502; RRID: AB_493302
Biotin-conjugated rat anti-PLVAP	Biolegend	Cat#120504; RRID:AB_493304
Goat anti-GFR α 1	R&D	Cat#AF560; RRID:AB_2110307
Rabbit anti-SOX3	GeneTex	Cat#GTX129235; RRID:AB_2885934
Goat anti-SOX3	R&D	Cat#AF2569; RRID:AB_2239933
Goat anti-PDX1	R&D	Cat#AF2419; RRID:AB_355257
Rabbit anti-CRE	CST	Cat#15036S; RRID:AB_2798694
Rat anti-E-Cadherin	Takara	Cat#M108
Alexa Fluor 488-conjugated rabbit anti-GFP	Thermo Fisher	Cat#A-21311; RRID:AB_221477
Goat anti-GFP	Abcam	ab6673; RRID:AB_305643
Alexa Fluor 488-conjugated mouse anti-BrdU	Thermo Fisher	Cat#B35139; RRID:AB_2536439
PECy7-conjugated rat anti-KIT	Biolegend	Cat#105814; RRID:AB_313223
Alexa Fluor 647-conjugated rat anti-CD9	Biolegend	Cat#124810; RRID:AB_2076037
Donkey polyclonal anti-rat IgG (Alexa Fluor 488)	Jackson ImmunoResearch	Cat#712-546-153; RRID:AB_2340686
Donkey polyclonal anti-rat IgG (Alexa Fluor 647)	Jackson ImmunoResearch	Cat#712-606-153; RRID:AB_2340696
Donkey polyclonal anti-rabbit IgG (Alexa Fluor 488)	Jackson ImmunoResearch	Cat#711-546-152; RRID:AB_2340619
Donkey polyclonal anti-rabbit IgG (Cy3)	Jackson ImmunoResearch	Cat#711-166-152; RRID:AB_2313568
Donkey polyclonal anti-goat IgG (Alexa Fluor 594)	Thermo Fisher	Cat#A32758; RID:AB_2762828
PE-conjugated goat anti-rat IgG	BD	Cat#550767; RRID:AB_393876
Biotin-conjugated rat IgG	Biolegend	Cat#400403; RRID:AB_326509
Control Alexa Fluor 647-conjugated goat IgG	Bioss antibodies	Cat#bs-0294P-A647
Chemicals, peptides, and recombinant proteins		
Alexa Fluor 488 NHS Ester	Thermo	Cat#A20181
Alexa Fluor 647 NHS Ester	Thermo	Cat#A20186
DyLight 488-conjugated streptavidin	Vector	Cat#SA-5488; RRID:AB_2336405
Brilliant Violet 421-conjugated streptavidin	Biolegend	Cat#405225
4OH-Tamoxifen	Sigma	Cat#H6278
Tamoxifen	Tronto Research Chemicals	Cat#T006000
EdU	Tokyo Kasei	Cat#E1057
BrdU	Tokyo Kasei	Cat#B1575
CF405M azide	Biotium	Cat#92092
Trypsin	SIGMA	Cat #59427C
Blocking One Histo	Nacalai Tesque	Cat #06349-64
Can Get Signal Solution 1&2	Toyobo	Cat#NKB-101
Type 1 collagenase	Worthington	Cat#CLS1
ISOGEN	Nippon Gene	Cat#311-02501
Recombinant human FGF2	PeproTech	Cat#100-18B
Recombinant human FGF5	R&D	Cat#237-F5
Recombinant rat GDNF	PeproTech	Cat#076-06121
Critical commercial assays		
Click-iT EdU Alexa Fluor 647 imaging Kit	Thermo Fisher	Cat#C10340
Single Cell-to-CT Kit	Thermo Fisher	Cat#4458237

(Continued on next page)

Continued

Reagent or resource	Source	Identifier
C1 Single-Cell Auto Prep Reagent kit	Fluidigm	Cat#100-6201
GE 96.96 Dynamic Array DNA Binding Dye Sample & Loading Reagent Kit	Fluidigm	Cat#100-3415
SuperScript VIL0	Thermo Fisher	Cat#11755050
Power SYBR Green PCR Master mix	Thermo Fisher	Cat#4367659
THUNDERBIRD SYBR qPCR Mix	Toyobo	Cat#QPS-201
SsoFast EvaGreen Supermix with Low ROX	Bio-Rad	Cat#172-5212

Deposited data

Single cell RNA sequencing data	(La et al., 2018)	accession number GSE107256
---------------------------------	-------------------------------------	----------------------------

Experimental models: Organisms/strains

<i>Plvap^{CreERT2}</i> mice	This study	N/A
<i>Sox3-CreER^{T2}</i> mice	This study	N/A
<i>Ngn3-CreERTM</i> mice	(Yoshida et al., 2006)	N/A
CAG-CAT-EGFP mice	(Kawamoto et al., 2000)	N/A
CAG-EGFP mice	(Okabe et al., 1997)	N/A
<i>GFRα1-GFP</i> mice	(Uesaka et al., 2007)	N/A
<i>Ngn3-EGFP</i> mice	(Yoshida et al., 2004)	N/A
<i>TⁿEGFP-CreERT2</i> mice	(Imuta et al., 2013)	N/A
Flipper mice	The Jackson Laboratory	JAX 003946
C57BL/6J mice	CLEA Japan, Japan SLC	N/A
DBA/2 mice	CLEA Japan	N/A

Recombinant DNA

IRES sequence from pEF1a-IRES-AcGFP1 vector	Takara	Cat #631971
---	--------	-------------

Software and algorithms

BD FACS Diva 6.1 and 8.0	BD	https://www.bdbiosciences.com/ja-jp/products/software/instrument-software/bd-facsdiva-software
Flowlogic 7	Milteny	https://www.miltenyibiotec.com/products/mac3-flow-cytometry/software/mac3quantify.html
PhotoshopCC 17.0.0	Adobe	https://www.adobe.com/jp/products/photoshop.html
Illustrator 20.0.0	Adobe	https://www.adobe.com/jp/products/illustrator.html
Affinity designer 1.8.4	AFFINITY	https://affinity.serif.com/ja-jp/
Microsoft Excel for Mac 15.32 and 16.46	Microsoft	https://www.office.com/
R (v4.0.3)	R Foundation for Statistical Computing	https://www.r-project.org/
scran (v1.12.1)	(Lun et al., 2016)	https://bioconductor.org/packages/release/bioc/html/scran.html
scater (1.18.6)	(McCarthy et al., 2017)	https://bioconductor.org/packages/release/bioc/html/scater.html
Seurat (v3.0.2)	(Stuart et al., 2019)	https://satijalab.org/seurat/
igraph (v1.2.4.1)	Gábor Csárdi	https://igraph.org/r/
pheatmap (v1.0.12)	Raivo Kolde	https://cran.r-project.org/web/packages/pheatmap/
slingshot (v1.9.1)	(Street et al., 2018)	https://github.com/kstreet13/slinsshot
bluster (v1.0.0)	Aaron Lun	http://www.bioconductor.org/packages/release/bioc/html/bluster.html
Codes for clonal simulations	This study	https://doi.org/10.5281/zenodo.5515900

Other

BAC Clone	Thermo Fisher	RP23-15016
C1 Single-Cell Auto Prep Array for PreAmp	Fluidigm	Cat#100-5480
96:96 dynamic array chips	Fluidigm	Cat#BMK-M10-96.96-EG

RESOURCE AVAILABILITY

Lead contact

Further information and requests for resources and reagents should be directed to and will be fulfilled by the lead contact, Shosei Yoshida (shosei@nibb.ac.jp).

Materials availability

The biological materials that support findings of this study are available upon reasonable request.

Data and code availability

- The data that support findings of this study are available upon reasonable request.
- The code used for biophysical modeling can be found on Zenodo (<https://zenodo.org/record/5515900#.YUci62ZKiqA>). DOI is listed in the key resources table.
- Any additional information required to reanalyze the data reported in this paper is available from the lead contact upon request.

EXPERIMENTAL MODEL AND SUBJECT DETAILS

Animals

CAG-CAT-EGFP, *GFR α 1-GFP*, *Ngn3-CreERTM*, *Ngn3-EGFP*, and *T^{nEGFP-CreERT2}* mice were previously described (Imuta et al., 2013; Kawamoto et al., 2000; Uesaka et al., 2007; Yoshida et al., 2006). *Flipper* mice (Farley et al., 2000) (JAX 003946) were obtained from The Jackson Laboratory. *Plvap^{CreERT2}* knock-in allele and *Sox3-CreER^{T2}* transgenic allele were generated in this study, as described in separate sections. *CAG-EGFP* mice were purchased from Japan SLC. Throughout, the mice were maintained under the C57BL/6 background (purchased from CLEA Japan or Japan SLC). The DBA/2 mice were purchased from CLEA Japan. All the mice analyzed in this study were male. The animals referred to as adult mice were at least two months of age. All the experiments and animal protocols were approved by the Institutional Animal Care and Use Committee of National Institutes of Natural Sciences, Animal Ethics Committee of Institute for Frontier Medical Sciences, Kyoto University, or the Institutional Animal Experiment Committee of the University of Tsukuba.

METHOD DETAILS

Generation of *Plvap^{CreERT2}* and *Sox3-CreER^{T2}* alleles

Plvap^{CreERT2} knock-in allele were generated by homologous recombination in embryonic stem cells as schematically shown in Figure S3A. A gene cassette composed of internal ribosome entry site (IRES, Takara), *CreER^{T2}* (Feil et al., 1997), and a neomycin resistance (*Neo*) gene flanked between a pair of *Frt* sites (a gift from Neal G. Copeland) was inserted into the 3'UTR region in the sixth exon of the *Plvap* gene, through gene targeting method in ES cells. *Neo* sequence was subsequently removed from the recombinant allele by mating with a *Flipper* mouse line (Farley et al., 2000) to obtain the *Plvap^{CreERT2}* allele, in which *CreER^{T2}* is expressed in PLVAP⁺ cells without affecting the *Plvap* expression. For generation of *Sox3-CreER^{T2}* transgenic allele (Figure S3J), a BAC clone (RP23-150I6) containing the entire *Sox3* gene, which is a single-exon gene, plus 211 kb flanking sequence was used. By using the recombineering in *E. coli* (Lee et al., 2001), the entire coding sequence of *Sox3* was replaced by the *CreER^{T2}* sequence (Feil et al., 1997) and the *FRT*-flanked *Neo* cassette; the *Neo* cassette was subsequently removed by inducible *Flp* in *E. coli*. Two *loxP* sites on BAC backbone were replaced with Zeocin and Ampicillin resistant genes. The recombined BAC was linearized by *PI-SceI* digestion, and was microinjected into the pronuclei of C57BL/6 mouse oocytes to gain transgenic animals.

Pulse-labeling experiments using *CreER-loxP* system

4OH-tamoxifen (Sigma), which was dissolved sequentially in ethanol, dimethyl sulfoxide and then sesame oil, was intraperitoneally injected into appropriate mice. The following combinations of 4OH-tamoxifen dose and recipient animals were used: two consecutive doses of 2.0 mg each with a 7 hours of interval into *Plvap^{CreERT2/+};CAG-CAT-EGFP* mice for experiments in Figures 2A, 2C, 2G, and 2H; a single dose of 0.6 mg 4OH-tamoxifen into *Plvap^{CreERT2/+};CAG-CAT-EGFP* mice for experiments in Figures 3A–3G; a single dose of 0.5 mg into *Sox3-CreER^{T2};CAG-CAT-EGFP* mice for experiments in Figures 2A, 2D, 2F–2H, and 3H–3K. For precise comparison of the percentage of pulse-labeled cells by *Sox3-CreER^{T2}*, two days after the pulse, one of the testes was removed from the individual mice, and ten days after the pulse, remaining testis was removed and analyzed. For experiment in Figures S4E, a single dose of 0.33 mg 4OH-tamoxifen was injected into *Ngn3-CreERTM;CAG-CAT-EGFP* mice. For experiments in Figures 2A, 2E, 2G, and 2H, *Ngn3-CreERTM;CAG-CAT-EGFP* mice were orally injected with two doses of 2.0 mg tamoxifen (Tronto Research Chemicals), dissolved in sesame oil, every other day.

No background recombination was detected in *Plvap^{CreERT2/+};CAG-CAT-EGFP* adult mice. Regarding *Sox3-CreER^{T2};CAG-CAT-EGFP* adult mice, background recombination was observed, but only infrequently. Specifically, 13 patched from a total of

Cell Reports

Article



1700 mm-long seminiferous tubules per adult testis were observed without tamoxifen injection. 11 of them included differentiating cells only with no GFR α 1⁺ cells, while the other two contained GFR α 1⁺ cells. Such a low level of recombination would present only a negligible impact on the results of the pulse-labeling experiments.

S-phase labeling with BrdU and/or EdU

Mice were injected with 0.5 mg of EdU (Tokyo Kasei) solved in sterile PBS once to determine the S-phase content in X, Y and Z fractions (Figures 4A and S4L). To determine the S-phase content in each stage of the seminiferous epithelial cycle (Figure 4E), the same dose was injected twice with a 7.5-hour interval. For continuous labeling with BrdU (Tokyo Kasei) (Figures 4B and S4M), intraperitoneal injection of 1 mg BrdU was followed by administration through drinking water (0.8 mg/ml) for variable time periods. For dual labeling of BrdU and EdU (Figure 4C), we continuously gave BrdU mice for 0.5 days as above. After various intervals, the mice were intraperitoneally injected with 0.5 mg of EdU twice at a 6-hour interval before euthanized 6 hours after the last injection of EdU.

For BrdU detection, untangled seminiferous tubules that were fixed and stained with primary and secondary antibodies in whole mount (as described in separate sections) were re-fixed with 4% PFA for 1 hour, treated with Trypsin (1:50 dilution, SIGMA) at 37°C for 30 minutes, and incubated with 2N HCl for 40 minutes. After washed thoroughly, the specimens were incubated with Alexa Fluor 488-conjugated mouse anti-BrdU antibody overnight.

For EdU detection, testicular sections and the untangled tubules following immunostaining of PLVAP, SOX3, GFR α 1, and BrdU, were stained with EdU using CF405M azide (Biotium) or Alexa Fluor 647 azide in combination with reaction buffers included in Click-iT EdU Alexa Fluor 647 imaging Kit (Thermo) according to the manufacturer's instructions.

Dual-pulse labeling experiment with BrdU and 4OH-tamoxifen

Plvap^{CreERT2/+};CAG-CAT-EGFP mice were intraperitoneally injected with 0.5mg of 4OH-tamoxifen and 1mg BrdU, following by administration of BrdU through drinking water (0.8mg/ml) for 16 hours. After varying duration of intervals, the seminiferous tubules were processed to whole-mount immunostaining for BrdU, PLVAP, and GFP, as described in separate section.

Antibodies used for immunostaining and FACS

The following antibodies were used for immunostaining: rat anti-PLVAP (with dilution by 1:100, Biolegend, 120501), goat anti-GFR α 1 (0.5 μ g/ml, R&D, AF560), goat anti-GFR α 1 (1 μ g/ml, R&D, AF560) conjugated with Alexa Fluor 647 NHS Ester (Thermo, A20186), rabbit anti-SOX3 (1:800, GeneTex, GTX129235), goat anti-SOX3 (1:1000, R&D, AF2569), goat anti-PDX1 (0.5 μ g/ml, R&D, AF2517), rabbit anti-CRE (1:400, CST, 15036), Alexa Fluor 488-conjugated rabbit anti-GFP (1:1000, Thermo, A-21311), goat anti-GFP (Abcam, ab6673) conjugated with Alexa Fluor 488 NHS Ester (Thermo, A20181), and Alexa Fluor 488-conjugated mouse anti-BrdU (1:100, Thermo, B35139). Secondary antibodies were Alexa Fluor- or Cy3-conjugated from Thermo or Jackson ImmunoResearch and used at 1:1000 dilutions.

The following antibodies were used for FACS: Biotin-conjugated rat anti-PLVAP (1:100, Biolegend, 120504), rat anti-E-Cadherin (1:300, Takara, M108), PECy7-conjugated rat anti-KIT (1:200, Biolegend, 105814), Alexa Fluor 647-conjugated rat anti-CD9 (1:1000, Biolegend, 124810), goat anti-GFR α 1 (1 μ g/ml, R&D, AF560) conjugated with Alexa Fluor 647 NHS Ester (Thermo, A20186), PE-conjugated goat anti-rat IgG (1:250, BD, 550767), biotin-conjugated rat IgG (1:100, Biolegend, 400403), and Alexa Fluor 647-conjugated goat IgG (1 μ g/ml, Bioss antibodies, bs-0294P-A647). Biotin-conjugated rat anti-PLVAP were detected with DyLight 488- (1:3000, Vector, SA-5488) and Brilliant Violet 421-conjugated streptavidin (1:1500, Biolegend, 405225).

Immunofluorescence staining of testicular sections

To prepare paraffin sections (Figures 4D and 4E), the testes were fixed with 4% PFA overnight and embedded in paraffin. For cryosections (Figures 1E, S2A–S2C, S3B–S3E, S3I, and S3K–S3N), the testes were fixed in 4% paraformaldehyde (PFA) in PBS for 2 hours, equilibrated in 20% sucrose/phosphate buffered saline, and then embedded in OCT compound (Tissue Tek). The paraffin sections following antigen retrieval with citrate buffer (10 mmol/l, pH6.0 at 100°C for 10 min), or the cryosections were blocked with Blocking One Histo (Nacalai Tesque) for 1 hour at RT and then incubated with primary antibodies diluted in 4% donkey serum/Can Get Signal Solution 1 (Toyobo) for 2 hour at RT. After washing with PBS containing 0.05% tween 20 (PBST), the sections were incubated with Hoechst 33342 and secondary antibodies diluted in 4% donkey serum/Can Get Signal Solution 2 (Toyobo) for 2 hour at RT. Slides were mounted in PermaFluor Aqueous Mounting Medium (Lab Vision Corporation); confocal microscopy was performed using a Leica TCS SP8 confocal system. Tiled images (Figures 1E and 1F) were generated with PhotoshopCC and LAS X software. Determination of the stage of seminiferous epithelial cycle was made on adjacent sections, which were stained with periodic acid Schiff's reagent and hematoxylin.

Whole-mount immunofluorescence

Untangled seminiferous tubules were fixed in 4% PFA for 1 hour, dehydrated through successive 7-min incubations in 25%, 50%, 75%, and 100% methanol in PBST on ice and then incubated in 100% methanol for 30 minutes. After rehydrated in graded methanol, washed in PBST, and blocked in PBST containing 4% donkey serum for 1 hour, the tubules were incubated with primary antibodies for 2 hours at RT, and, following brief wash with PBST, incubated with secondary antibodies for 2 hours. To stain GFP protein, Alexa Fluor 488-conjugated rabbit or goat anti-GFP antibodies were used, after blocking with species-matched rabbit or goat serum (4%,

in PBS). Whole seminiferous tubules (Figures 2B and 2C) were photographed under M165FC stereomicroscope (Leica). For confocal microscopy, specimens were mounted in PBST and observed using a Leica TCS SP8 confocal system.

Especially, to detect GFP (Figure 3) and BrdU (Figures 4B and S4M) in X, Y, and Z compartments under SP8 confocal microscopy, untangled seminiferous tubules were stained with the following combinations of antibodies and fluorochromes: BrdU and GFP, Alexa fluor 488; SOX3, Cy3; GFR α 1, Alexa fluor 594; PLVAP, Alexa fluor 647. Our Leica TCS SP8 confocal system can detect Alexa fluor 488 (BrdU and GFP) and Alexa fluor 647 (PLVAP) excited by 488 nm and 638 nm lasers without spillover to different channels, respectively. But, because of the limitation of the availability of lasers equipped with our Leica TCS SP8 confocal system, Cy3 (SOX3) and Alexa fluor 594 (GFR α 1) were simultaneously excited by the 552 nm laser. To overcome this limitation and discriminate SOX3 and GFR α 1 expression, we took advantage of different emission spectra of Cy3 and Alexa fluor 594 and the localization of SOX3 (nucleus) and GFR α 1 (plasma membrane). We detected Cy3 and Alexa Fluor 594 signals with emission wavelengths of 553-569nm and 607-656nm, respectively, to avoid spillover from Alexa Fluor 594 (GFR α 1) into Cy3 (SOX3) channel, enabling to detect SOX3-specific signal. Despite the spillover from Cy3 into Alexa Fluor 594 channel, we could judge GFR α 1 expression based on its localization on cells membrane.

For quantification of protein expression level in Figures S2F and S2G, confocal images were obtained from whole-mount seminiferous tubules of *Ngn3-EGFP* mice, stained for GFR α 1, SOX3, and EGFP. The value of signal intensity of each cell in Figure S2G was calculated as the sum of pixel value obtained from ellipse-shaped region of interests (ROIs) that were placed to include the cell nucleus for SOX3 staining (with major and minor axes of 13.0 and 12.5 μ m, respectively) and the cell body for GFR α 1 and *Ngn3-EGFP* staining (with major and minor axes of 17.9 and 14.9 μ m, respectively), using LAS X software (Leica). Background signals were obtained from regions negative for all of GFR α 1, SOX3, and *Ngn3-EGFP* signals using the same experimental setup.

Flow-cytometry and cell sorting

Flow cytometric experiments and cell sorting were performed using FACSAria SORP, FACSAria II (BD), and MA900 (SONY), using antibody-stained testicular single cell suspensions prepared as described below. Data were analyzed with FACSDiva software (BD) and FlowLogic (Milteny).

To prepare single cells suspension used in single-cell multiplexed qRT-PCR (Figure S1A), testes of adult *GFR α 1-EGFP* mice were first incubated in PBS containing 5 mg/ml Type 1 collagenase (Worthington), 0.17 mg/ml DNase I (Sigma) at 37°C for 15 min, followed by dissociation by vigorous pipetting and incubate at 37°C for another 10 min. Then, the single cell suspension was washed four times by centrifugation at 200 \times g for 5 minutes and resuspended in 10 mL PBS.

For single cell preparation to use qRT-PCR analyses (Figures 1B, 1C, and S1E–S1G), testes of wild-type adult mice were dissociated without collagenase treatment to protect GFR α 1 protein from digestion, given the identified sensitivity to collagenase (Figure S1C). The tunica albuginea of the testes of adult C57BL/6 mice were removed, and the seminiferous tubules were minced with surgical scissors, and suspended in 10 mL PBS and then collected by centrifugation at 200 \times g for 10 s to remove differentiated cells released from the cut ends of the tubule fragments, which do not sediment in this centrifugation condition. The resultant tubule fragments were treated with 0.17 mg/ml DNase I and 2.0 mg/ml Hyaluronidase (Tokyo Kasei) in PBS for 12 minutes at 37°C, and dissociated into single cells by vigorous pipetting. Suspended single cells and the tubule fragments were separated by 70 μ m nylon mesh (BD). Because many GFR α 1⁺ cells still remained in the tubule fragments, the fragments were resuspended in PBS, dissociated by vigorous pipetting, and single cells were recovered four times to get high yield of GFR α 1⁺ cells. The resultant single cell suspension was washed four times by centrifugation at 200 \times g for 5 minutes and resuspended with 10 mL PBS.

The resultant single cells were stained with rat anti-E-Cadherin primary antibody (Takara, M108) and PE-conjugated goat anti-rat IgG secondary antibody (BD, 550767). Then, the cells were incubated in the solution containing purified rat IgG (0.1 mg/ml) for blocking and cocktails of antibodies listed below: PECy7-conjugated anti-KIT and Alexa fluor 647-conjugated anti-GFR α 1, and biotin-conjugated anti-PLVAP antibodies (Figure 1B); PECy7-conjugated anti-KIT and Alexa fluor 647-conjugated anti-GFR α 1, and Brilliant Violet 421-conjugated anti-PLVAP (Figures S4A–S4D); PECy7-conjugated anti-KIT and Alexa fluor 647-conjugated anti-CD9 antibodies (Figure S1A); PECy7-conjugated anti-KIT and Alexa fluor 647-conjugated anti-GFR α 1 antibodies (Figure S1C); or PECy7-conjugated anti-KIT and biotin-conjugated anti-PLVAP antibodies (Figure S1D). Biotin-conjugated antibodies were further labeled with Brilliant Violet 421-conjugated streptavidin (Thermo, S21374) (Figure 1B) or DyLight 488-conjugated streptavidin (Vector, SA5488) (Figure S1D).

First, cells were analyzed after removing small and large debris in FSC-A versus SSC-A gating, doublets in FSC-W versus FSC-H gating, and PI⁺ dead cells. Then, desired cell population was collected in gates determined based on reporter expression and/or antibody staining.

Quantitative RT-PCR of sorted cell fractions

For qRT-PCR analyses in Figures 1C, S1E–S1G, S2H–S2M, S4C and S4D, total RNA was isolated from sorted cell fractions using ISOGEN (Nippon Gene), and cDNA was synthesized using SuperScript VILO (Thermo) according to the manufacturer's instructions. qRT-PCR analysis was performed with a Step One Plus (Thermo), a LightCycler 480 System, or a LightCycler 96 System (Roche) using Power SYBR Green PCR Master mix (Thermo) and THUNDERBIRD SYBR qPCR Mix (Toyobo). The values for each gene were normalized to the relative quantity of *Gapdh* mRNA in each sample. The primers are listed in Table S2.

Cell Reports

Article



Transplantation

FACS-sorted subpopulations of A_{undiff} from *CAG-EGFP* mice (Figure 2J) were proceeded for transplantation as described (Ogawa et al., 1997). Briefly, the sorted cells were injected into the seminiferous tubules of the host C57BL/6 mice which had been intraperitoneally treated with busulfan (44mg/kg; Wako) at least 5 weeks before the transplantation for depletion of endogenous germ cells. After two months, the host testes were excised, and their seminiferous tubules were immunostained in whole-mount for GFP and PLVAP. The detailed information including the number of injected cells and raw counts of the colonies are summarized in Figure S3S.

Single-cell multiplexed qRT-PCR

For single-cell multiplexed qRT-PCR (Figures S1A and S1B), preamplified cDNA templates were prepared from FACS-sorted fractions from *GFR α 1-EGFP* mice. The sorted single cells (a 10:1 mixture of $EGFP^+E\text{-Cadherin}^+CD9^+KIT^{\text{low}}$ and $EGFP^+E\text{-Cadherin}^+CD9^+KIT^{\text{low}}$ A_{undiff} fractions) were captured individually on a C1 Single-Cell Auto Prep Array for PreAmp (Fluidigm) designed for 10- to 17-um cells using a Fluidigm C1 system (Fluidigm). Cell lysis, cDNA synthesis, and preamplification were performed using Single Cell-to-CT Kit (Thermo), C1 Single-Cell Auto Prep Reagent kit, and specific primers for arbitrarily selected target genes (Table S2). qPCR was performed on a 96:96 dynamic array chips (Fluidigm) using GE 96.96 Dynamic Array DNA Binding Dye Sample & Loading Reagent Kit (Fluidigm), and SsoFast EvaGreen Supermix with Low ROX (Bio-Rad), in a Biomark HD system (Fluidigm) platform, following the manufacturer's instructions. The Raw data from 60 cells were analyzed in RStudio software (<https://www.rstudio.com/>). The detection limit of Ct value was set to 24; results are expressed as $2^{(24 - Ct)}$.

Reanalysis of single-cell RNA-seq data

QC and removing contaminants

We obtained and re-analyzed single-cell RNA-seq data of A_{undiff} (in particular, $Plzf\text{-mCherry}^+CD9^+KIT^+$ fraction) from a previous study (La et al., 2018) deposited in the Gene Expression Omnibus (GEO) (GSE112880). The raw dataset consists of two biological replicates with 3,798 cells for replicate 1 and 5,626 cells for replicate 2. For quality control, only cells with $200 < \text{number of genes} < 5000$ and percentage of mitochondrial transcripts $< 20\%$ were considered for further analysis. In addition, genes expressed in less than 3 cells were excluded. Unique Molecular Identifiers (UMIs) were normalized by a deconvolution method using R package *scrn* (v1.12.1) (Lun et al., 2016). PCA combined with technical noise modeling was applied to the normalized data for dimension reduction, which was implemented by function *denoise_PCA* in *scrn*. The PCA result was used for non-linear dimension reduction based on two-dimensional Uniform Manifold Approximation and Projection (UMAP) implemented in function *runUMAP* (default parameter used) of R package *scater* (v1.18.6) (McCarthy et al., 2017). The distribution of cells was visualized in UMAP using R package *Seurat* (v3.0.2) (Stuart et al., 2019). In UMAP, the two biological replicates overlapped well with each other, confirming reproducibility of the data and removing concern about batch effect. Then we performed clustering for the data based on Louvain community detection algorithm (Blondel et al., 2008) implemented by function *buildSNNGraph* (k-nearest neighbor = 13) of *scrn* and function *cluster_walktrap* of R package *igraph* (v1.2.4.1). As a result of clustering, all cells were classified into 17 clusters. Among the 17 clusters, 7 were identified as contaminants such as peritubular myoid cells (*Acta2*-positive), Sertoli cells (*Igfbp7*, *Sparc*, *Cldn5*, *Tmsb4x*-positive), and spermatids (*Tekt4*, *Prr1*, *Tnp2*-positive) and were excluded for further analysis.

Dimension reduction and clustering

To remove potential bias due to cell cycle signature, we performed cell cycle regression and linear and non-linear dimension reduction using *Seurat*. Specifically, we calculated S and G2/M scores using function *CellCycleScoring* and applied them for regressing out cell cycle effect using function *ScaleData*. Then, we selected and used 3,000 most variable genes for linear dimension reduction by applying function *RunPCA*. The top 30 PCs were selected and used for non-linear dimension reduction implemented by function *RunUMAP*. We then performed Louvain clustering (k-nearest neighbor = 7) again for the data without cell cycle effect, resulting in 13 clusters. To understand the identity of the clusters, we checked expression of 25 marker genes related to self-renewal and differentiation, as well as somatic cells in the clusters (Figure S1J). As 3 clusters expressed marker genes for differentiating spermatogonia (*Stra8*, *Kit*-positive), spermatocytes (*Sycp1* and *Sycp3*-positive) and macrophages (*Lyz2*, *Cd14*-positive); these 3 clusters were removed for further analysis.

Annotating cell clusters into five cell states

To understand population structure of the single-cell RNA-seq data, we annotated the cell clusters based on marker gene expression and merged them into a few cell states by referring to the theoretical model. To this end, we examined the relationships between the 10 clusters by constructing a graph (Figure S1K) where nodes are clusters and edges are weighted based on \log_2 -(ratio of observed total weights to expected total weights of edges between cells in different clusters). The ratio was calculated by function *pairwiseModularity* of R package *bluster* (v1.0.0). Based on this graphical abstraction of the clusters, we classified the 10 clusters into 5 cell states, including *Plvap*-high (X), Y1, Y2, *Sox3*-high (Z), and *Ngn3*-high, in the following steps. First, we could observe three groups of clusters in the graphical abstraction: clusters 1, 2, 7; clusters 3, 5, 10; clusters 9, 11, 12, 13. This grouping was also largely supported by expression of marker genes for self-renewal and differentiation (Figure S1J). However, we noted that clusters 5 and 7 were located between clusters 1, 2 and clusters 3, 10. In addition, clusters 5 and 7 expressed the marker genes at intermediate levels between clusters 1, 2 and clusters 3, 10. Thus, we decided to consider clusters 5 and 7 as a transitional state between clusters 1, 2 and

clusters 3, 10. Furthermore, based on heterogeneity of gene expression, we considered clusters 5 and 7 as distinct states. In summary, the 5 cell states are as follows (Figure S1L): clusters 1 and 2 for *Plvap*-high (X); cluster 7 for Y1; cluster 5 for Y2; clusters 3 and 10 for *Sox3*-high (Z); and clusters 9, 11, 12, and 13 for *Ngn3*-high.

Pseudotime analysis

To understand the lineage relationship, pseudotime analysis was performed for the 5 cell states using function *slingshot* of R package *slingshot* (v1.9.1) (Street et al., 2018) with a starting clusters as *Plvap*-high. As a result, *slingshot* suggested two lineage paths: lineage 1) *Plvap*-high (X) -> Y1 -> *Sox3*-high (Z) -> *Ngn3*-high; lineage 2) *Plvap*-high (X)-> Y1 -> *Sox3*-high (Z)-> Y2 -> *Plvap*-high (Z). To characterize the cell states at molecular level in an unbiased manner, we examined gene expression patterns specific to each of the cell states along the pseudotime trajectories. To this end, for each trajectory, highly expressed genes (FDR < 0.01 and $\log_2(\text{fold-change}) > 0.3$) for each of the cell states belonging to the trajectory were calculated using one-sided t test and pooled together, which resulted in 1,077 genes for lineage 1 and 950 genes for lineage 2 (Table S3). For each gene, \log_2 -transformed normalized UMIs were z-transformed and smoothed using rolling mean along a pseudotime trajectory with a window size (i.e., 378 for lineage 1, 389 for lineage 2) of 5% of total number of cells belonging to the trajectory. As a result, two heatmaps of gene expression were generated for the two lineages (Figures S1M and S1N).

Effect of FGFs and GDNF on cultured spermatogonia

Primary germline stem (GS) cell culture derived from 8-day-old DBA2 mice were established and maintained in the presence of 10 ng/ml FGF2 (PeproTech) and 10 ng/ml GDNF (PeproTech), on a feeder layer of mouse embryonic fibroblasts (MEFs), as reported previously (Kanatsu-Shinohara et al., 2003). To assess the effect of FGF2 and GDNF, one day after 3×10^5 GS cells were seeded per well (using 12-well plates), culture media were switched to those with or without FGF2 (10 ng/ml) and/or GDNF (10 ng/ml). Following another 24 hours cultured in these conditions, the GS cells were collected using FACS, based on their low SSC/low FSC property compared to the high SSC/high FSC signals in MEFs. To assess the effects of FGF5 (R&D) in addition to FGF2 and GDNF, GS cells were depleted for FGF2 and GDNF for 1 day, and then the culture media were switched to those with or without FGF2 (10ng/ml), FGF5 (100ng/ml), and GDNF (10ng/ml). Eight hours after incubation, the GS cells were collected using FACS.

Statistical analysis

As described in the legends to figures, throughout, data are displayed as mean \pm SD or SEM and sample size are also displayed in each legend. The significance of the difference of experimental groups was assessed by unpaired two-tailed Student's t test, using Microsoft Excel (Microsoft). Violin and dot plots were generated with R package and Excel, respectively. A level of $p < 0.05$ was considered to be statistically significant. No statistical method was used to predetermine the sample size.